Trends of mean temperatures and warm extremes in northern tropical Africa (1961-2014) from observed and PPCA-reconstructed time series

Vincent Moron, Boutheina Oueslati, Benjamin Pohl, Sandra Rome, Serge Janicot

▶ To cite this version:

Vincent Moron, Boutheina Oueslati, Benjamin Pohl, Sandra Rome, Serge Janicot. Trends of mean temperatures and warm extremes in northern tropical Africa (1961-2014) from observed and PPCA-reconstructed time series. Journal of Geophysical Research: Atmospheres, 2016, 121 (10), pp.5298-5319. 10.1002/2015JD024303 . halshs-02153184

HAL Id: halshs-02153184
https://shs.hal.science/halshs-02153184v1

Submitted on 12 Jun 2019

AGU PUBLICATIONS

JGR

Journal of Geophysical Research: Atmospheres

RESEARCH ARTICLE

10.1002/2015JD024303

Key Points:
- Assessment of the regional-scale warming in tropical Africa from 1961 to 2014
- Low-frequency variations primarily viewed as a fingerprint of the global warming
- High-frequency variations primarily viewed as a delayed response to Pacific ENSO

Supporting Information:
- Supporting Information S1

Correspondence to:
V. Moron,
moron@cerege.fr

Citation:
Moron, V., B. Oueslati, B. Pohl, S. Rome, and S. Janicot (2016), Trends of mean temperatures and warm extremes in northern tropical Africa (1961–2014) from observed and PPCA-reconstructed time series, *J. Geophys. Res. Atmos.*, *121*, 5298–5319, doi:10.1002/2015JD024303.

Received 2 OCT 2015
Accepted 23 APR 2016
Accepted article online 27 APR 2016
Published online 19 MAY 2016

Trends of mean temperatures and warm extremes in northern tropical Africa (1961–2014) from observed and PPCA-reconstructed time series

Vincent Moron[1,2], Boutheina Oueslati[3], Benjamin Pohl[3], Sandra Rome[4], and Serge Janicot[5]

[1]Aix-Marseille University, UM 34 CNRS, CEREGE, Aix en Provence, France, [2]IRI, Columbia University, PalisadesNew York, USA, [3]CRC, UMR 6282 Biogéosciences, CNRS/Université de Bourgogne–Franche-Comté, Dijon, France, [4]LTHE UMR 5564 CNRS/UJF/IRD/G-INP, Université Grenoble Alpes, Grenoble, France, [5]UMR7159 LOCEAN, Sorbonne Universités UPMC-CNRS-IRD-MNHN, Paris, France

Abstract Trends in daily maximum (TX) and minimum (TN) temperatures and indices of warm extremes are studied in tropical North Africa, west of the eastern African highlands, from 1961 to 2014. The analysis is based on the concatenation and cross-checking of two observed databases. Due to the large number of missing entries (~25%), a statistical infilling using probabilistic principal component analysis was applied. Averaged over 90 stations, the linear trends of annual mean TX and TN equal respectively +0.021 °C/yr and +0.028 °C/yr. The frequency of very hot days ($TX > 35°C$) and tropical nights ($TN > 20°C$), as well as the frequency of daily TX and TN above the 90th percentile (p90) ("warm days" and "warm nights"), roughly follows the variations of mean TX and TN, respectively. Heat spells of TX or $TN > p90$ are often short (usually $<$2–3 days), and the interannual variation of their mean duration is noisier than for the other indices. Nevertheless, heat spells tend to last longer, with almost constantly positive anomalies since the mid-1990s. The trends in March–June, the warmest season across the Sahelian and Sudanian belts, show similar variations as annual means. Overall, the local-scale warming in annual temperatures, and in March–June, may be viewed merely as a simple shift of the probability distribution function of daily TX and TN. The correlations between the thermal indices and the 2 m temperatures suggest that the low-frequency ($>$8 years) variations may be viewed as a regional-scale fingerprint of the global warming, with largest correlations in the tropical Atlantic and Indian basins, while the high-frequency ($<$8 years) variations should be mostly viewed as a delayed remote impact of El Niño–Southern Oscillation (ENSO) events over the region, with warm (cold) anomalies tending to follow warm (cold) ENSO events.

1. Introduction

It has long been recognized that the Earth is experiencing a large-scale warming, due to increasing greenhouse gases caused by anthropogenic activities. For decades, most analyses of long-term climate change focused mostly on monthly, seasonal, and annual mean temperatures. At the global scale, a warming trend of 0.10°C ± 0.02°C per decade was recorded over the 1901–2012 period and even reached up to 0.26°C ± 0.05°C per decade between 1979 and 2012 [*Hartmann et al.*, 2013]. This global warming trend was accompanied by consistent changes in climate extremes (i.e., increase in either frequency and duration and amplitude of heat peaks/waves for example), which usually have more visible and larger impacts on ecosystems, economies, and societies than the mean changes [e.g., *Easterling et al.*, 2000a, 2000b; *Coumou and Rahmstorf*, 2012; *Cowan et al.*, 2014]. One such dramatic impact was exemplified by the 2003 European summer heat wave [*Trigo et al.*, 2005; *Cowan et al.*, 2014], which caused between 22,000 and 70,000 heat-related deaths [*Schär and Jendritzky*, 2004; *Coumou and Rahmstorf*, 2012]. Such a high number of deaths is rare in developed countries of western and central Europe where capacities in mitigation and adaptation are considered to be more efficient compared to developing countries. More recently, similar devastating heat waves occurred in Pakistan and India during boreal spring 2015.

Several studies have analyzed the time variation of climate extremes at the global scale [*Groisman et al.*, 1999; *Frich et al.*, 2002; *Christidis et al.*, 2005; *Caesar et al.*, 2006; *Alexander et al.*, 2006; *Brown et al.*, 2008; *Donat and Alexander*, 2012; *Donat et al.*, 2013a; 2013b], but with usually large gaps in the tropics, especially throughout tropical Africa and South America (see, for example, Figure 2 of *Brown et al.* [2008]). We focus here over such an understudied area, namely, tropical Africa, north of the Equator, and east of the eastern African highlands during a 54 year period (1961–2014) through a concatenation of two data sets totaling 90 stations (from Global Historical Climate Network (GHCN) daily and Global Summary of the Day (GSOD)). Previous analyses on tropical Africa included only few countries, especially in southern and eastern Africa [*King'uyu et al.*, 2000; *New et al.*, 2006; *Aguilar et al.*, 2009], but also located in Arabic speaking countries from the northern Sahelian fringes to the Mediterranean coast [*Donat et al.*, 2014].

This work offers a comprehensive analysis of the spatiotemporal variations of mean temperatures (and their warm extremes) since the 1960s over tropical north Africa. Climatologically, this area is very warm, mostly due to a combination of three main factors: low latitude, low elevation, and continentality landmass. The low latitudes receive a large amount of incoming solar radiation, with two annual peaks south of the tropic of Cancer. Elevation higher than 1000 m is rare in tropical north Africa, except in the Sahara desert. The size of the African continent north of the Equator, together with the general easterly trade winds, inhibits advection of cool oceanic air from the tropical North Atlantic toward the interior of the Sahelian and Sudanian belts. Low-level monsoon flow blows from equatorial and tropical South Atlantic from March to November. However, the potential cooling effect from the low-level moisture is reduced over the Sahelian and Sudanian belts in June–September after a 750–1000 km travel across the Guinean Africa. Strong incoming solar radiation leads to extreme high temperatures (i.e., daily maximum temperature (TX) is usually over 40°C, while daily minimum temperature (TN) is well above the threshold used to define "tropical" nights, that is 20°C) in boreal spring over Sudanian and Sahelian belts, just before the monsoon. Clouds and evaporation tend to decrease TX during the rainy season. The second annual peak of temperature occurring after the rainy season in September–November is weaker than the springtime peak, at least due to its timing near and after the autumn equinox, except for narrow coastal areas along the tropical North Atlantic.

Intergovernmental Panel on Climate Change [2013] concluded that 21st century warming due to anthropogenic forcing will be large in Africa, which is likely to increase the number and duration and amplitude of heat waves, especially in arid and semiarid regions of West Africa [*Pachauri and Reisinger*, 2008; *Christensen et al.*, 2007; *Stocker et al.*, 2013]. At the regional scale of the Central Sahel and Guinean zone, *Ringard et al.* [2016] have already shown that the rising trends in TX and TN over the past 60 years are more pronounced than those of the other regions of the West African domain. These positive trends are consistent with *Fontaine et al.* [2013] based on National Centers for Environmental Prediction/National Center for Atmospheric Research (NCEP/NCAR) Reanalyses [*Kalnay et al.*, 1996], who showed a significant warming (1°C–3°C) for the period 1979–2011 over Sahara and Sahel. They associated the warming trend with more frequent warm temperatures over the 90th percentile, as well as longer durations and higher occurrences of heat waves. In boreal autumn and spring (October-November-December and April-May-June), the warming trends are larger in TN than in TX, which suggest a decrease in the daily temperature ranges as observed on the global scale [*Braganza et al.*, 2004]. This is, however, not verified in summer (July-August-September), when TX increases more rapidly than TN in the Sahel [*Rome et al.*, 2015; *Ringard et al.*, 2016].

Our analysis is based on station observations rather than previously explored gridded data sets [*Collins*, 2011; *Fontaine et al.*, 2013; *Cook and Vizy*, 2015]. Moreover, the focus on the warm tail of the more recent observations is due to its critical relevance for societal and health impacts there, where the current mean state may already approach dangerous thresholds from the physiological point of view [*Sherwood and Huber*, 2010] and may even soon potentially exceed these thresholds in case of amplified warming [*Cook and Vizy*, 2015]. The paper is organized as follows. Section 2 describes the databases used and the selection of thermal indices partly following the guidelines of the Expert Team on Climate Change Detection and Indices (Expert Team on Climate Change Detection and Indices, 2013, http://www.clivar.org/clivar-panels/etccdi). The trends for annual and March–June (MAMJ) means (i.e., the warmest season for the Sahelian and Sudanian belts) and warm extremes are analyzed in section 3. Section 4 presents the relationships between regional-scale thermal variations and global temperatures and analyzes the potential predictability of MAMJ mean and extreme temperatures from tropical sea surface temperatures (SST). Section 5 discusses the main results of this paper. Concluding remarks are provided in section 6.

2. Data and Methods

2.1. Extraction, Concatenation, and Validation of Daily Temperatures

Daily TX and TN are extracted from two databases: the "Global Surface Summary of the Day" (GSOD version 7 [*Lott et al.*, 2008]) and the daily "Global Historical Climate Network" (GHCN version 2 [*Menne et al.*, 2012])

(a) Stations in GSOD & GHCN

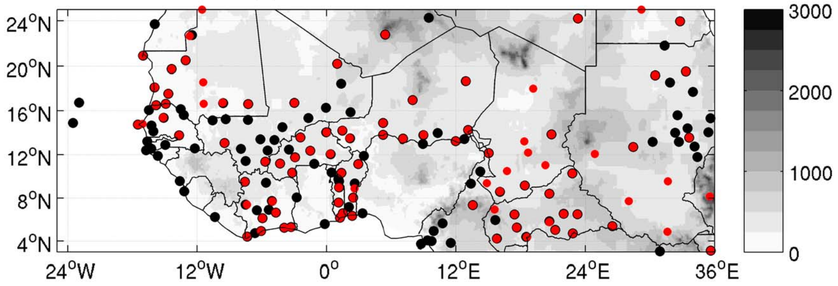

(b) available stations

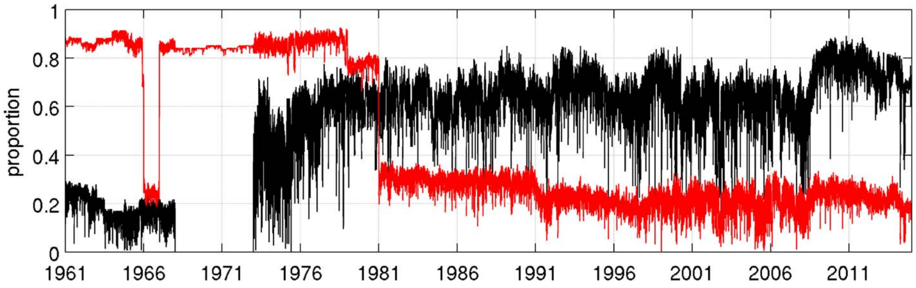

(c) 90 Stations

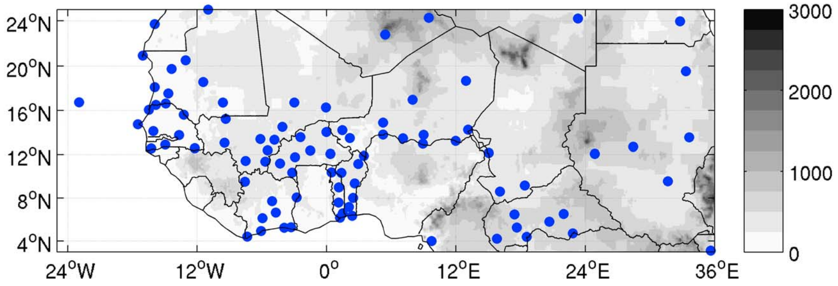

(d) available stations

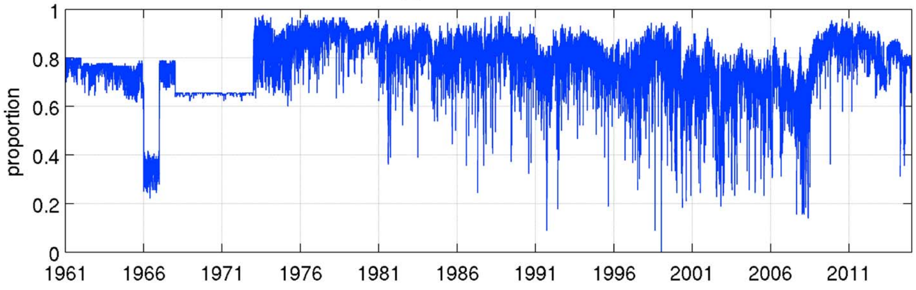

Figure 1. (a) Location of the GSOD (large black dots) and GHCN (small red dots) stations having at least 3650 available daily records of maximum and minimum temperature in 1961–2014. (b) daily availability of maximum temperature (TX) and minimum temperature (TN) in both databases (black curve for GSOD, red curve for GHCN). (c) Location of the 90 stations from the concatenation of GSOD and GHCN database having at least 30 available years of maximum and minimum temperature in 1961–2014. (d) Daily availability of TX and TN in the final database.

on the spatial window shown in Figure 1a. GSOD is produced by the National Climatic Data Center and consists of 18 daily surface meteorological variables, including TX and TN. One hundred forty-seven stations from GSOD and 94 stations from GHCN that have at least 10 years of observations (not necessarily continuous) between 1961 and 2014 are extracted first (Figure 1a). GSOD data include long and continuous gaps before 1973 (Figure 1b), while the GHCN database is well documented between 1961 and 1981 (Figure 1b).

Table 1. Frequency of Missing Entries Ranked by the Lengths of Consecutive Missing Entries Expressed as Absolute (and Relative as Percentage of the Total in Parenthesis) Number of Sequences and Days Included in These Sequences

	TX Sequences	TX Days	TN Sequences	TN Days
1–5 days	80,490 (91.8 %)	130,681 (30.1 %)	80,589 (91.8 %)	131,314 (30.1 %)
6–15 days	5,300 (6)	45,686 (10.5)	5,328 (6.1)	45,959 (10.5)
16–31 days	1,039 (1.2)	22,525 (5.2)	1,034 (1.2)	22,393 (5.1)
32–90 days	554 (0.6)	27,595 (6.4)	556 (0.6)	27,854 (6.4)
91–365 days	241 (0.3)	44,383 (10.2)	246 (0.3)	45,455 (10.4)
>365 days	81 (<0.1)	163,230 (37.6)	81 (<0.1)	163,239 (37.4)
Total	87,705	434,100	87,834	436,214

We first removed values considered as spurious in the database, i.e., daily observation warmer or colder than the mean ± 4 standard deviations (SD) from the climatological daily mean. Daily means and SD have been computed for each station on a 5 day running window using available entries from 1961 to 2014. Our analyses are based either on counts of hot days and warm nights or indices based on the 90th percentile computed either on all days or from the running 5 day window (see section 2.2 for the definition of the warm indices). There are 138 (TX and TN in GSOD), 121 (TN in GHCN), and 123 (TX in GHCN) available daily temperature values for each 5-day sample (a far larger sample is available when the 90th percentiles is computed using all days). There are between 12 and 14 values within the 90th percentile. We can thus assume that removing sometimes the highest annual values would not dramatically change the 90th percentile. The cumulative probability of a standardized anomaly of 4 SD is indeed >0.9999 in a Gaussian distribution, thus well above 0.90. In fact, only 0.07% (TX GSOD), 0.02% (TX GHCN), 0.06% (TN GSOD), and 0.01% (TN GHCN) of daily entries exceeding +4 SD are discarded from the following analyses.

Seventy-four stations that meet the above criteria are available in both databases, while 20 stations are available in GHCN only, while 73 are available in GSOD only. The average of the local-scale correlations for the common period (in mean, 5306 common days for TX and 5105 common days for TN) is equal to 0.96 ± 0.04 for TX and 0.93 ± 0.06 for TN. The average of root-mean-square error for the common period is equal to 0.78°C ± 0.49°C for TX and 1.07°C ± 0.69°C for TN. Since it is not possible to identify the most reliable record due to the absence of any metadata in GSOD and GHCN databases, the average of GSOD and GHCN data is computed when both databases are available. Then 93 stations (out of a total of 167) having at least 30 years of record, not necessarily consecutive, are retained. The spatial coverage is heterogeneous, omitting Nigeria and Ghana and also most of Sahara (Figure 1c). Daily entries of 23.7% (TX) and 23.8% (TN) are missing in this set (Figure 1d).

Table 1 shows the distribution of missing data through the length of consecutive missing entries. There are 81 sequences lasting at least 365 days, corresponding to 428 years-stations (=8.5% of the whole set of 54*93 yearly TX and TN sequences), while 2692 (TX) and 2691 (TN) years-stations have less than 10% of daily missing entries.

Missing entries are filled with a probabilistic principal component analysis (PPCA [*Tipping and Bishop*, 1999]). PPCA is based on a latent variable model, which could be established on available data only. The quality of reconstructions is tested using a Monte Carlo approach. The most challenging case, that is when a full year is missing, is tested. A set of 10%, 20%, 30%, 40%, and 50% missing entries are randomly created by year-station blocks separately for TX and TN. A PPCA is next used to estimate these data from the eigenbasis computed on the available entries only. The skill of the reconstructions is computed as correlation between reconstructed and observed indices related to the 90th percentile of TX and TN. The first index is the annual frequency of daily TX or TN above the 90th percentile (computed on the whole available data). The second index is the annual mean length of spell of daily TX or TN above this 90th percentile. Note that the observed missing entries are replicated at the same space-time locations in the reconstructions to not bias the comparison between observed and filled sequences and that the correlations are computed only on the 2692 (TX) and 2691 (TN) years-stations having less than 10% of daily missing entries.

This is repeated 50 times starting from a different random set of missing entries. The reconstruction is tested by using the 5, 10, 20, 30,…, 93 eigenvectors of the PPCA. Correlations between reconstructed and observed TX and TN saturate near 30 eigenvectors (not shown). Table 2 shows the mean correlations, averaged over 50 replicates, for both indices defined above. The second column shows the mean correlations between the

Table 2. Mean Correlation (on 50 Replicates) Between Observed and PPCA-Reconstructed Interannual Variations of Two Indices Related to the 90th Percentile Defined From All Days (P90) (Annual Counts of Daily TX—Second and Third Columns—or TN—Sixth and Seventh Columns—Exceeding the 90th Percentile and Mean Length of Spells of Consecutive TX—Fourth and Fifth Columns—or TN—Eighth and Ninth Columns—Exceeding the 90th Percentile) for 10%–50% of Missing Entries Randomly Created as Annual Blocks[a]

	Annual TX > P90	Only Filled Annual Anomalies	Mean Length of TX > P90	Only Filled Annual Anomalies	Annual TN > P90	Only Filled Annual Anomalies	Mean Length of TN > P90	Only Filled Annual Anomalies
10%	0.95	0.72	0.92	0.55	0.93	0.68	0.88	0.47
20%	0.90	0.70	0.85	0.53	0.87	0.69	0.78	0.45
30%	0.85	0.70	0.78	0.52	0.81	0.68	0.69	0.44
40%	0.80	0.68	0.71	0.50	0.74	0.67	0.61	0.42
50%	0.72	0.64	0.62	0.45	0.67	0.64	0.53	.39

[a] The first column of each couple (i.e., second, fourth, sixth, and eighth columns) gives the mean correlation, spatially averaged over the 93 stations, using all yearly sequences having at least 329 available entries, while the second column (i.e., third, fifth, seventh, and ninth columns) gives the mean correlation over the filled yearly sequences having at least 329 available entries only and considering all stations together.

observed and observed + reconstructed time series, spatially averaged over the 93 stations and then averaged over the 50 replicates, for the annual frequency of daily TX > 90th percentile. The correlation decreases logically as the proportion of missing entries increases, but it equals 0.9 for 20% of missing entries. The correlations decrease slightly for the annual frequency of daily TN > 90th percentile (sixth column of Table 2). Restricting the correlations to filled year-stations only logically decreases the correlations between observations and reconstructions, but they remain >0.69 for 20% of missing entries (Table 2). Overall, the correlations are weaker for the mean length of spells >90th percentile, especially for TN (Table 2). This is consistent with a lower signal-to-noise ratio of the variables dealing with the mean length of heat spells as detailed below (see Figure 4 and section 3.2). PPCA may also fail to reproduce the exact chronology of TX and TN > 90th percentile. Both biases are indeed related, since noisy variations could not be accurately reproduced with a method as PPCA relying on the covariant information among variables (i.e., stations). The TX and TN missing entries are then estimated as the mean of 10 replicates of PPCA using the leading 30 eigenvectors.

The last step consists in evaluating the homogeneity of climatic time series. A classical approach is based on well-known statistical tests such as the Standard Normal Homogeneity, Buishand range, Pettitt, or Von Neuman ratio tests [*Alexandersson and Moberg*, 1997; *Klein Tank and Können*, 2003; *Wingaard et al.*, 2003]. These four tests suppose under the null hypothesis that the observations are independent and identically distributed. The first three tests are capable of locating a single break under the alternative hypothesis [*Wingaard et al.*, 2003]. The Von Neumann ratio test assumes under the alternative hypothesis that the time series is not randomly distributed, but the null hypothesis may be systematically rejected when a trend is present as in contemporaneous temperature records. Rejecting the null hypothesis would not be an indication of any error in that case.

A different approach to estimating heterogeneity in a single time series is based on multilayer regressions, able to detect more than one break in a time series ([*Wang*, 2008; *Ruggieri*, 2012]—used in *Aguilar et al.* [2009] We use here the Bayesian method of *Ruggieri* [2012], which provides uncertainty estimates on both the number and location of change points. A posterior probability is computed objectively assessing the uncertainty surrounding the optimal solution: an abrupt change gives a single posterior probability close to 1, while a progressive acceleration of increase (or decrease) gives a value ≤0.5 distributed on several consecutive dates [*Ruggieri*, 2012]. The test is applied here to mean annual TX and TN. Only one TN (zero for TX) change point has a posterior probability of ≥0.5 in 2009 in Linguere (Senegal). This change point is related to an abrupt 2°C drop between 2009 and 2014 and the previous years (not shown). Therefore, this station is discarded from the network.

The mean correlations of annual TX and TN between a central station and those located in a N-km radius are analyzed to detect stations exhibiting distinct variability than surrounding stations. A first trial using a 250 km radius shows that two stations—Diourbel in Senegal and Bamako/Senou in Mali—have a mean correlation lower than the mean (0.76) minus 3 SD (0.18) for annual mean TN with 7 and 3 surrounding stations, respectively. Diourbel shows a large increase of interannual variance after 1984, while Bamako/Senou shows an unexpected decreasing trend in TN from 1980 (while TX increases there, as elsewhere) (not shown). Such unexpected behavior does not appear for annual TX. A 250 km correlation radius is too small for most of Saharan stations, which are more distant from each other compared to the Mali and Senegal station density.

Table 3. Summary of the 12 Warm Indices[a]

Index	Index abbreviate	Unit
Mean daily maximum temperature (TX)	mTX	°C
Mean daily minimum temperature (TN)	mTN	°C
"*hot day*" (=day with TX > 35°C)	HotD	Count in day
"*tropical night*" (=night with TN > 20°C)	TropN	Count in day
Percentage of days with TX > percentile 90% on running 5 day windows (=*warm days*)	TX90p	%
Percentage of nights with TN > percentile 90% on running 5 day windows (=*warm nights*)	TN90p	%
Mean length of spells of TX > percentile 90% on running 5 day windows (="*warm spell duration* on TX)	WSD TX	Length in day
Mean length of spells of TN > percentile 90% on running 5 day windows (=*warm spell duration* on TN)	WSD TN	Length in day
Mean length of spells of TX > percentile 90% on all days (=*warm spell duration* on TX, second definition)	WSD2 TX	Length in day
Mean length of spells of TN > percentile 90% on all days (=*warm spell duration* on TN, second definition)	WSD2 TN	Length in day
Mean length of spells of TX and TN > percentile 90% on running 5 day windows (=*warm spell duration* on TX and TN)	WSD	Length in day
Mean length of spells of TX and TN > percentile 90% on all days (=*warm spell duration* on TX and TN, second definition)	WSD2	Length in day

[a] Some of them are based on 90th percentile either computed on running 5 day windows (p90) or on the entire record (P90).

We increase the radius to 500 and 1000 km, but it does not reveal any other doubtful stations than Linguere, Diourbel, and Bamako/Senou. Therefore, all following analyses are based on a set of 90 stations and 54 years of daily TX and TN (Table S1 and Figures 1c and 1d).

2.2. Definition of Temperature Extremes

In this study, we are interested in warm extremes. All possible indices (Expert Team on Climate Change Detection and Indices (ETCCDI) [*Zhang et al.*, 2011] are not always relevant for the Sahelian/West African case. For example, "summer" days defined as daily TX > 25°C occur on almost all days within that region (350 to 365 d/yr on average, depending on the stations), except for the coolest regions along the tropical North Atlantic coast and for some mountainous stations (as Tamanrasset in southern Algeria). All indices are computed yearly and for the MAMJ season, corresponding to the warmest months over most of the region.

We first consider two absolute extremes, which are relevant for impact studies: the number of "hot" days (HotD: TX > 35°C) and tropical nights (TropN: TN > 20°C). HotDs are of primary importance since, when air temperatures exceed 35°C, the human body can only maintain normal core body temperature by sweating [*Kjellstrom*, 2009; *Sherwood and Huber*, 2010]. A TX of 35°C should be considered as a conservative estimate of such threshold, since temperatures are usually warmer than TX under the sun within this region. TropNs are equally important since they do not allow for thermal stress recovery after warm days.

We then consider relative indices from the tail of the distribution by computing the 90% percentile of a running 5 day window centered on the target day (referred as p90). The percentiles are computed over the entire record. A first index is the proportion of days exceeding this threshold (warm days—TX90p—and warm nights—TN90p—according to *Peterson et al.* [2001]). The warm spell duration index is defined by ETCCDI as the number of days with TX > p90 in intervals of at least six consecutive days. Such duration is rarely observed over our network, especially for TN (see section 3.1). As a result, we compute the mean duration of warm spells with TX > p90 (WSD TX), TX > p90 (WSD TN) from a 1 day duration, and also for the sequences of days for which TX and TN are both > p90 (WSD), to account for heat spell combining warm days and warm nights. All mean durations are also estimated by considering a single 90th percentile computed on all days for each station (referred as P90). These indices are abbreviated respectively as WSD2 TX, WSD2 TN, and WSD2 and emphasize the warmest period of the annual cycle (primarily the boreal spring across Sahelian and Sudanian belts). Thus, a total of 12 indices (summarized in Table 3) are used in this work.

3. Spatiotemporal Variability of Temperatures and Heat Extremes

3.1. Mean Annual Cycle and Warm Extremes

Figure 2 shows a hierarchical clustering of the annual cycle of TX and TN. The daily means of TX and TN are computed for each station, and all daily values are normalized versus the grand mean (across stations and days, i.e., +33.7°C for TX and +21.5°C for TN) to distinguish different phases of the annual cycle as well as "warm" versus "cold" locations. The six-cluster solution is chosen since it leads to contiguous clusters and interpretation is straightforward.

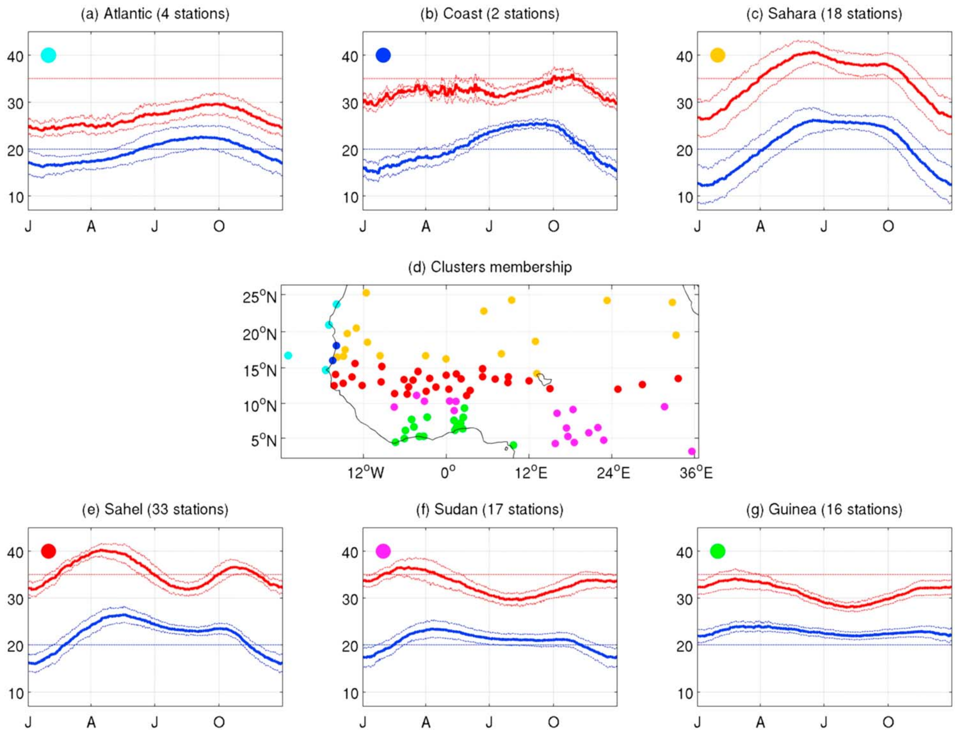

Figure 2. (a–g) Hierarchical clustering of the joint mean annual cycle of TX and TN. Absolute TX and TN (in °C) at each station are normalized by the grand mean of TX (+33.7°C) and TN (+21.5°C). The distance used in hierarchical clustering is Pearson correlation, and the average distance is used to cluster iteratively the stations. The red and blue full curves in Figures 2a, 2b, 2c, 2e, 2f, and 2g show mean TX and TN spatially averaged over the stations belonging to each cluster (Figure 2d) with the ± one standard deviation among these stations shown as dashed lines. The red and blue horizontal dashed lines in Figures 2a, 2b, 2c, 2e, 2f, and 2g indicate the thresholds to define very hot days (TX > 35°C) and tropical nights (TN > 20°C), respectively.

Two clusters include only four and two coastal stations along the Atlantic coast and in the Cape Verde archipelago (Table S1). Note that these two clusters are still not merged in the five-cluster solution, i.e., indicative of distinct behavior (not shown). TX are relatively cool there, especially for “Atlantic” cluster (Sal, Dakar/Yoff, Nouadhibou, and Daklha; see Table S1 and Figure 2a), due to the cooling effect of the sea, including the Canary upwelling, which seems narrowly restricted to the coast and Cape Verde archipelago due to prevalent offshore trade winds along the tropical North Atlantic all year long. Eighteen “Saharan” stations (Figure 2c) show warmer temperatures with HotDs (210 in mean) and TropNs (212 in mean) occurring continuously from late March to late October. The thermal conditions are rather similar over the “Sahelian” belt, running from the interior of Senegal to Southern Sudan around 12°N–15°N (Table S1 and Figure 2e). The corresponding 33 stations have 191 HotDs and 264 TropNs per year on average. The first thermal peak around May is warmer than the second peak around October (Figure 2e), primarily due to the zenith angle of incidence, leading to a larger amount of incoming solar radiation in May than in October, but also due to drier soils by the end of the dry seasons. TX tends to decrease southward over the Sudanian belt (93 HotDs and 245 TropNs per year in mean over the 17 stations; Figure 2f), and the June–September wet season coincides with the coolest season for TX (respectively, TN) (respectively, boreal winter). The Guinean coast (Figure 2g) shows a very flat annual cycle due to its near-equatorial latitude, especially for TN, consistently between 20°C and 23°C (there are 362 TropNs, while only 24 HotDs occur per year on average across the 16 stations).

Figure 3 shows the long-term mean of various thermal indicators (Table 3). mTX (Figure 3a) and P90 of TX (Figure 3e) clearly peak across the Sahelian belt. The mTX zonal gradient is large between coastal Senegal and Mauritania and the interior (Figure 3a). P90 of TX (Figure 3e) is near or over +40°C over the whole Sahara and Sahelian belts. Warm indices based on TN vary much less in space than those based on TX (Figure 3), but they still tend to peak across the Sahelian belt, especially for the P90 of TN (Figure 3f), with a second maximum over Guinean stations.

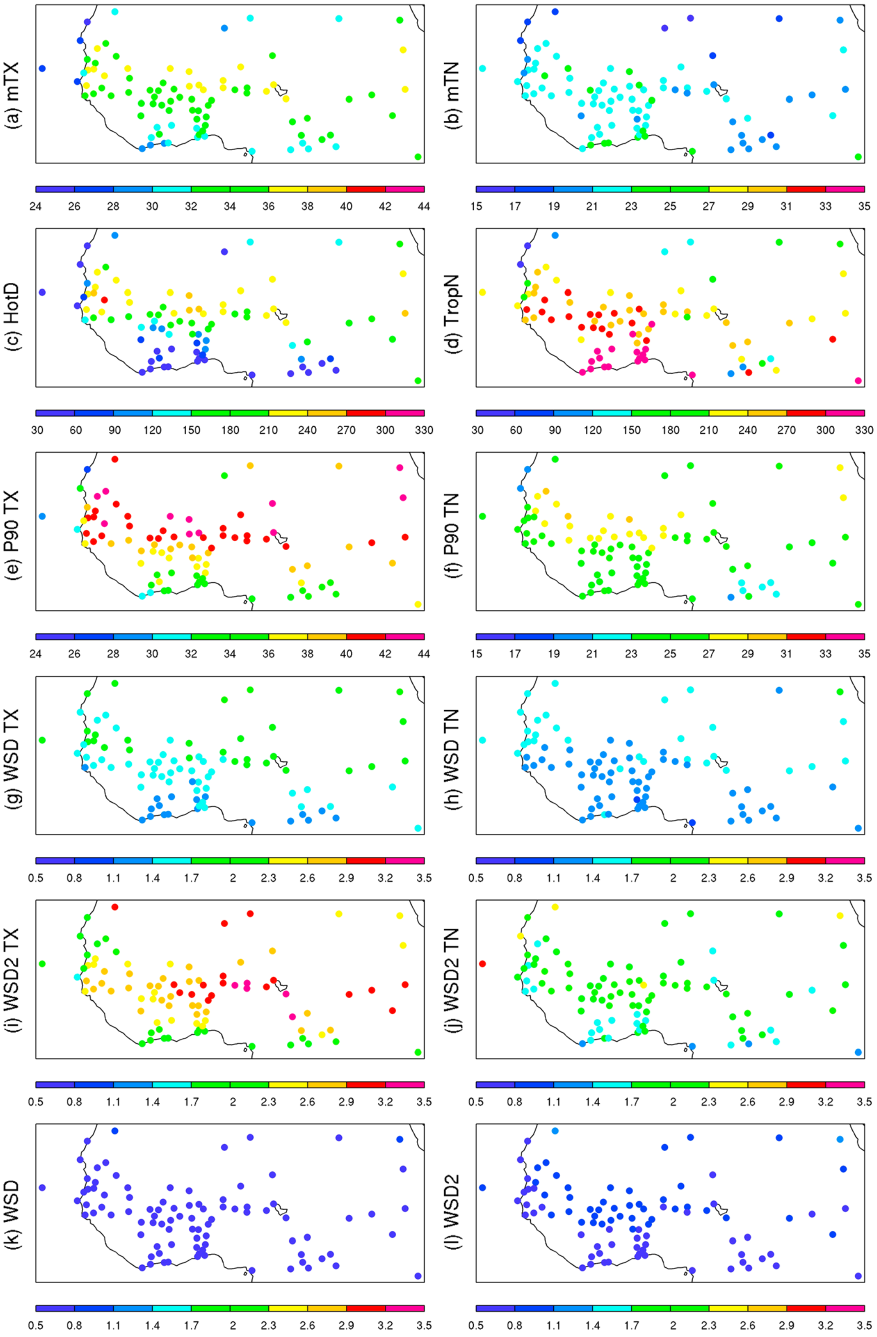

Figure 3. Mean annual values of 12 thermal indices defined from daily TX and TN: (a) mean TX; (b) mean TN, both in °C; (c) number of hot days (i.e., TX > 35°C) and of (d) tropical nights (i.e., TN > 20°C) as number of days; (e) 90th percentile of TX considering all days in °C; (f) 90th percentile of TN considering all days in °C; (g) mean duration of spells of TX > 90th percentile of TX computed on running 5 day window; (h) mean duration of spells of TN > 90th percentile computed on running 5 day window; (i) mean duration of spells of TX > 90th percentile computed on all days; (j) mean duration of spells of TN > 90th percentile computed on all days; (k) mean duration of spells of TX and TN > 90th percentile of computed on running 5 day window; (l) mean duration of spells of TX and TN > 90th percentile computed on all days.

The mean duration of spells of TX > p90 (WSD TX; Figure 3g) is equal to 1.6 days, with only 2.4% of the total sequences lasting at least six consecutive days. Such a short mean duration is due to the large proportion of non-consecutive occurrence of TX > p90, i.e., a large proportion of "spell" lasts only 1 day. Similarly, using TN > p90 (WSD TN; Figure 3h) leads to a mean duration of 1.4 days. Considering both TX and TN > p90 (WSD; Figure 3k) leads to even shorter spells (0.6 day in mean) since 84% of the sequences include either TX or TN > p90, such

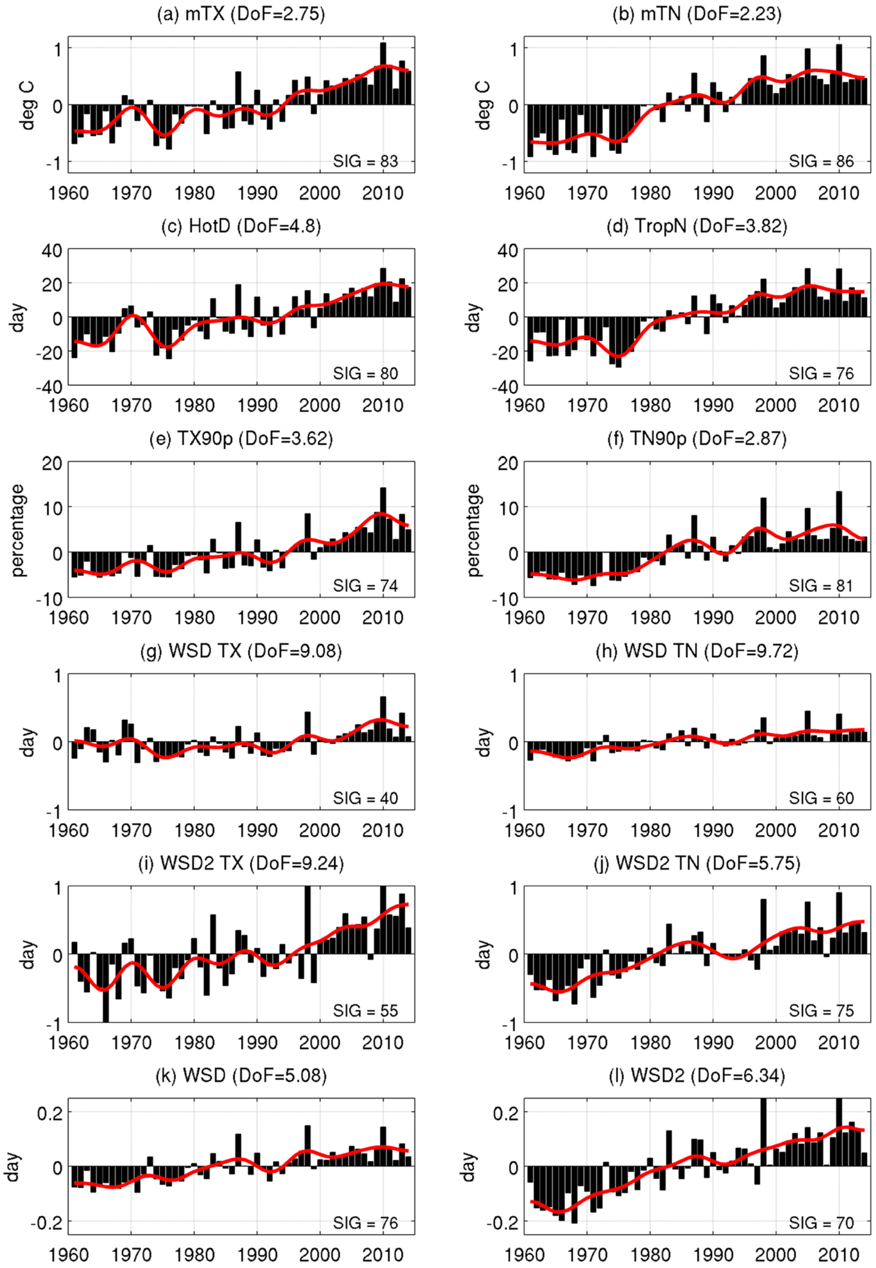

Figure 4. Interannual variations of the 12 thermal yearly indices defined in Table 3 (except for (e) TX90p, which is the proportion of TX > p90 computed on running 5 day window and (f) TN90p, which is the proportion of TN > p90 computed on running 5 day window). The bars are the spatial average of local-scale yearly anomalies standardized to zero mean on 1961–2014. The number of degrees of freedom (DoF) [*Fraedrich et al.*, 1995; *Moron et al.*, 2007] is indicated in the title of each panel. The number of DoF varies between 1 for perfect spatially covariant variations (i.e., correlations between stations equal systematically 1 or −1) to 31–32 for independent variations. "SIG" is the number of stations for which the linear slope is positive and significant at $p = 0.05$ according to a Student's t test.

length being counted as 0.5 day. Only 205 sequences last at least 12 consecutive TX and TN (i.e., at least six consecutive days) > p90. Using P90 instead of p90 slightly increases the mean duration of heat spells to respectively 2.6 (WSD2 TX; Figure 3i), 1.9 (WSD2 TN; Figure 3j) days, and 0.8 day (WSD2; Figure 3l) because it focuses on the warmest period of the year, thus slightly clustering together warm days and nights. As a consequence, the mean duration of warm spells (Figures 3g–3l) is short, since many years do not record any warm spell (or several warm "spells" lasting 1 or 0.5 day), especially when both TX and TN exceed p90 or P90 (Figures 3k and 3l). The mean WSD TX (Figure 3g) is close to 1.2–1.4 days over the Guinean and Sudanian belts. WSD TX increases up

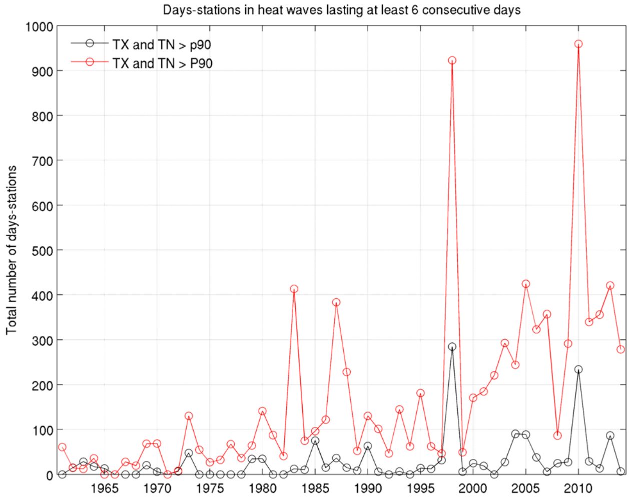

Figure 5. Total annual number of days-stations included in heat waves lasting at least six consecutive days (i.e., at least 12 consecutive TX and TN above the 90th percentile (p90) computed on 5 day running windows in black line and above the 90th percentile (P90) computed on all days in red line).

to 1.7–2.3 days northward (Figure 3g). The geographical pattern of WSD2 TX (Figure 3i) is similar, with longer durations ($>$2.5 days north of 7°N–8°N). Considering sequences of TN and TX $>$ p90 or P90 (Figures 3k and 3l) decreases the mean duration to less than 1 day.

In summary, the entire study area is characterized by a very warm basic state, usually peaking just before the wet season that lasts from June to September. The northern Tropical Atlantic coast experiences a different local ($<$100 km from the coast) climate, with a relative cooling effect in spring and a larger peak after the monsoon retreat, due to the thermal inertia of the ocean. Over the Guinean belt, the two annual maxima are similar in amplitude, while over the Sahara, the absence of a wet season leads to a single long maximum around boreal summer.

3.2. Temporal Variations of Yearly (and MAMJ) Indices

The temporal variations are first analyzed through the spatial average of local-scale yearly anomalies calculated by removing the local mean (Figure 4). The time variations are overall consistent among the thermal indices with a larger signal-to-noise ratio (i.e., degree of freedom (DoF) [*Fraedrich et al.*, 1995; *Moron et al.*, 2007] close to 1) for TN indices (Figures 4b, 4d, 4f, 4h, and 4j) than for TX (Figures 4a, 4c, 4e, 4g, and 4i). The noise is larger for WSDs especially when TX and TN are individually considered (Figures 4g, 4h, 4i, and 4j). Considering the crossing of both TX and TX percentiles slightly reduces the noise (Figures 4k and 4l). The indices related to TX show negative anomalies until the late 1970s, or even the late 1980s, followed by a quasi-linear increase until the end of the period, 2010 often being the warmest year (Figures 4a, 4c, 4e, 4g, and 4i). The indices related to TN show a slightly different behavior with near-constant negative anomalies until the mid-1970s followed by an abrupt increase during the 1980s and 1990s, then stabilizing from 2000 onward. Three well-defined peaks occur in 1998, 2005, and 2010 (Figures 4b, 4d, 4f, 4h, and 4j).

If we consider only the frequency of days included in heat wave lasting at least six consecutive days (i.e., at least 12 consecutive TX and TN $>$ p90; black curve on Figure 5), they are also heavily clustered in the last 20 years (Figure 5). Sixty-five percent of the total number of these days occur from 1998 onward while 34% occur in 1998 and 2010 only. The correlation between the spatial average of WSD (Figure 4k) and the annual frequency of days in heat wave lasting at least six consecutive days (using TX and TN $>$ p90) is indeed large ($r = 0.67$, $p < 0.01$). The recent increase in heat wave days lasting at least six consecutive days since 1998 is even more spectacular when TX and TN $>$ P90 are both considered (red curve on Figure 5), with two extreme peaks already highlighted in 1998 and 2010, but also large maxima in 1983, 1987, 2005 and 2013 ($r = 0.85$, $p < 0.01$, with WSD2).

The above analyses are completed by an assessment of the changes in probability distribution function (PDF) of daily TN and TX in each station. Figure 6 summarizes the results through the proportion of stations having a significant difference at $p = 0.05$ (increase and/or warm anomaly in red and decrease and/or cold anomaly in blue). It is clear that TN and TX of the first (respectively last) 20 year period are significantly colder (respectively, warmer) than in random samples for most stations, but this warming is not systematically associated with changes in other statistical properties. For example, several stations show increased SD in 1995–2014 versus 1961–1980, but this increase is significant at $p = 0.05$ for ~30%–40% of the stations (TX and TN), and ~10% of the stations (in TN only) show on the contrary a significant decrease at $p = 0.05$ of their SD (Figure 6). The changes in skewness and kurtosis typically do not exceed $p = 0.05$ at local scale and are not systematic in sign

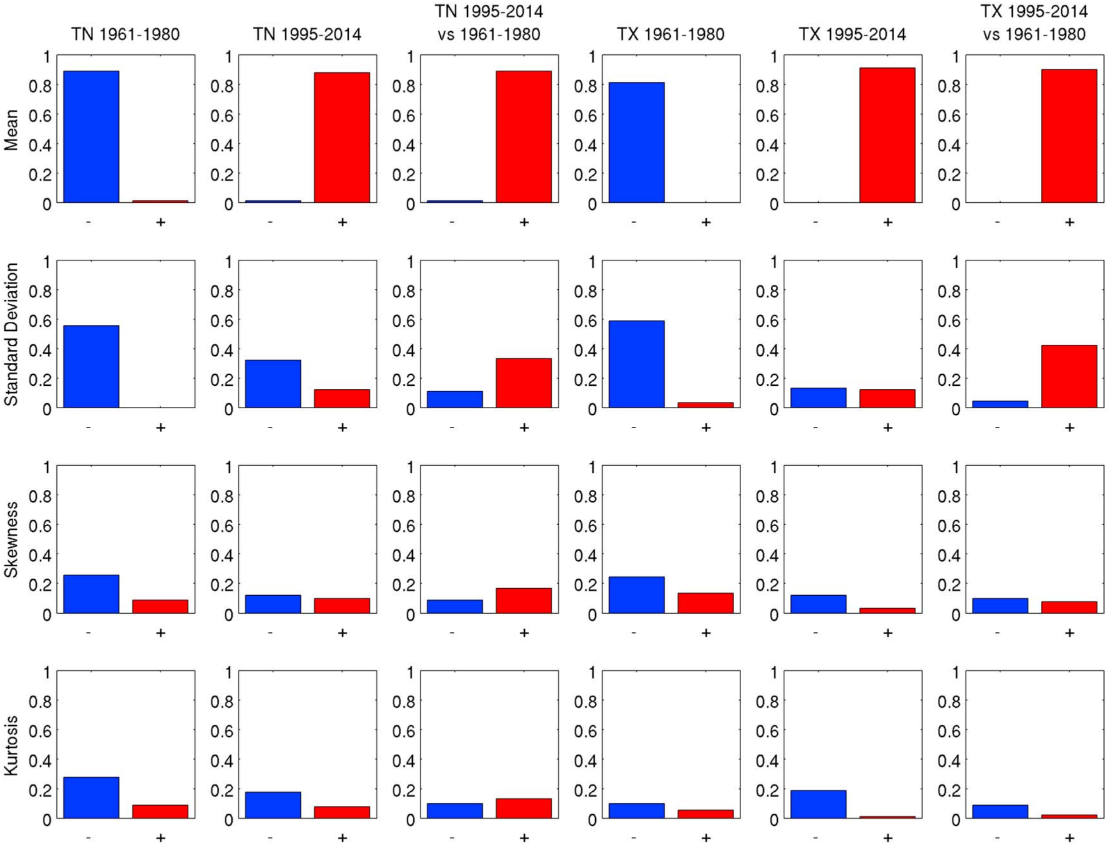

Figure 6. Proportion of stations where the PDF changes in and between 1961–1980 and 1995–2014 are significant at $p = 0.05$. The first row shows the change in mean, the second row, the change in standard deviation, the third row, the change in skewness, and the fourth row, the change in kurtosis. The three right hand-side columns show the changes in TX (for the first 20 years, the last 20 years and the difference between 1995 and 2014 minus 1961 and 1980), while the three left hand-side columns show the same changes for TN. For each panel, the blue and red bars indicate respectively the proportion of stations having a significant negative and positive anomaly (or change). All analyses are done on each stations and the significance is estimated with a Monte Carlo sampling of 20 years randomly chosen 1000 times (see text).

(Figure 6). Hence, the contemporaneous warming should be considered merely as a simple shift of the PDF without any systematic change in its shape.

All thermal indices are intrinsically, statistically, and physically related to mTX and mTN. Understanding the linearity and intensity of the relationships between mTX and mTN trends and those of related warm indices remain an interesting question that guides this paper. The answer to this question could help to empirically infer the future changes of warm indices from the projected changes in mTX and mTN. We computed the 1961–2014 linear trends of all indices on the whole set of 90 stations and plotted the slopes of mTX versus TX-related indices trends (Figures 7a, 7c, 7e, and 7g) and the slopes of mTN versus TN-related indices (Figures 7b, 7d, 7f, and 7h). For TX-related indices, there is a linear relationship between mTX and related indices. Comparing mTX and TX90p (Figure 7c) suggests that the increase of mTX is associated with a shift of the whole PDF of daily TX (i.e., the mean increase is quasi linearly related to more warm days), corroborating the results shown in Figure 6. The same relationship exists between the mTX warming and longer heat spells (Figures 7e and 7g). Such linearity is not as clear for thermal indices related to TN (Figures 7b, 7d, 7f, and 7h) with weaker slopes and more spread than for TX-related indices.

Figure 8 shows the slope and significance of local-scale linear trends spatially averaged over the nine regional-scale indices defined from Figure 2: the Atlantic, “Coast,” and “Guinea” stations constitute three groups, while the “Sahara,” “Sahel,” and “Sudan” clusters are split into distinct groups on each side of 5°E to analyze possible differences across longitudes. A large proportion of indices/regions show significant positive trends. The linear trends in mTX (Figure 8a) and mTN (Figure 8b) vary between ~ +0.1°C/decade to +0.3°C/decade (mTX) and +0.2°C/decade to +0.4°C/decade (mTN). This corresponds to an increase of ~ 1–9

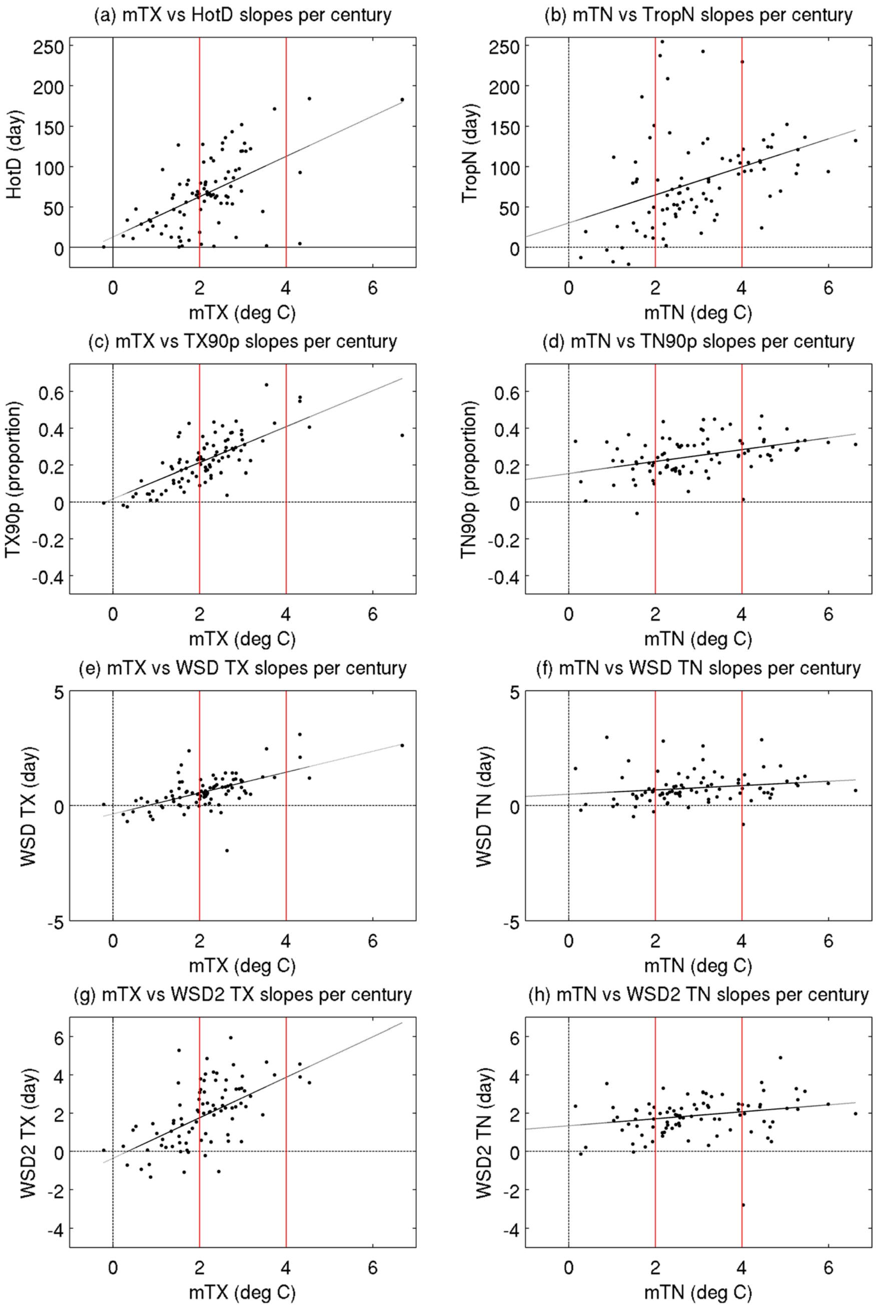

Figure 7. Scatterplots of the linear slope of mean TN (mTN in left column) and mean TN (mTX in right column) expressed as °C per century and various thermal indices related to either TX or TN (defined in Table 3); (a) HotD and (b) TropN (in day per century); (c) TX90p and (d) TN90p (in proportion per century); (e) WSD TX and (f) WSD TN (in day per century); (g) WSD2 TX and (h) WSD2 TN (in day per century). All slopes are computed using the annual values of the 90 stations shown as black dots. The least-square regression fit is shown as a black line.

HotDs/decade (Figure 8c) and of ~4–13 TropNs/decade (Figure 8d). The trends are less consistent for warm spell durations (Figures 8g–8l). Trends are usually not significant at $p = 0.05$ or negative for Western Sahara and the coastal region while they are positive and usually significant at $p = 0.05$ for Sahelian, Sudanian, and Guinean areas (Figures 8g–8l).

In summary, the trends are indicative of a long-term warming related to more "warm" and "hot" days and longer heat spells. The indices related to TN show larger linear slopes, but the temporal behavior is more step-like than for TX, with abrupt warming concentrated in late 1970s and in the 1990s. The 2001–2010 decade is the warmest,

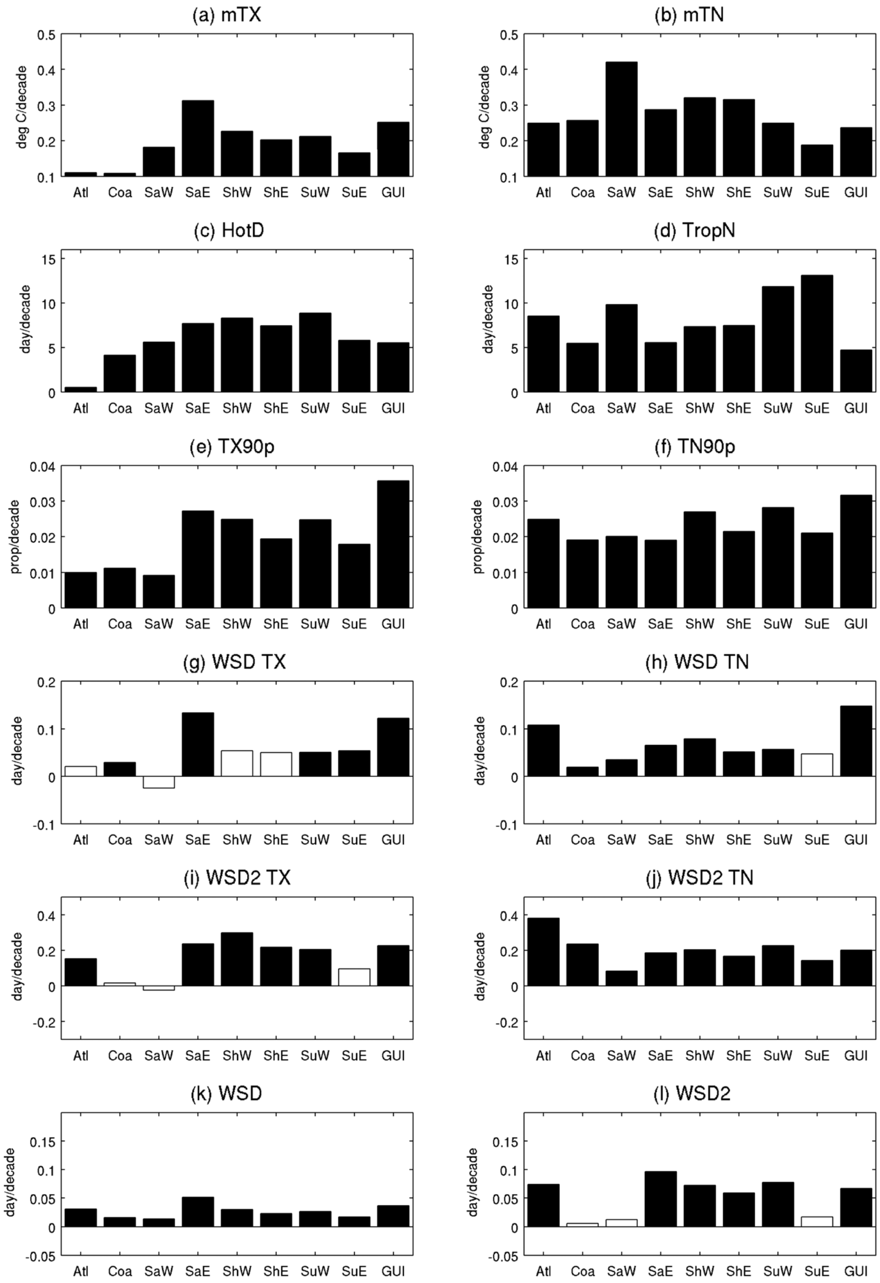

Figure 8. Mean rate (per decade) of linear trends computed on 1961–2014 on the 12 thermal indices defined in Table 3 and spatially averaged over the nine regions defined in Figure 2. The Saharan (Sa), Sahelian (Sh) and Sudanian (Su) clusters are splitted on each side of 5°E between a Westerly (W) and an Easterly (E) group. Filled bars indicate that at least 50% of the stations included in a given region show a positive trend significant at $p = 0.05$ according to a Student's *t* test.

and 2010 is usually the warmest year, followed by 2005 and 1998. Years 1998 and 2010 are also related to the largest number of days included in persistent heat waves, lasting at least six consecutive days.

We repeated the same analyses on the warmest season for the Sahelian and Sudanian belts, namely, the MAMJ season. The figures for the standardized anomaly indices, changes in the PDF, and linear trends for the nine spatial indices are reported in Figures S1–S3 in the supporting information. The temporal variability of the standardized anomaly indices (Figure S1) is highly similar to the annual one, even if DoF are larger than for annual values. This is expected due to the reduced temporal period (122 versus 365 days). The main difference is that increasing rates are usually higher in that season than for the entire year. The signal-to-noise ratio is smaller for HotD and

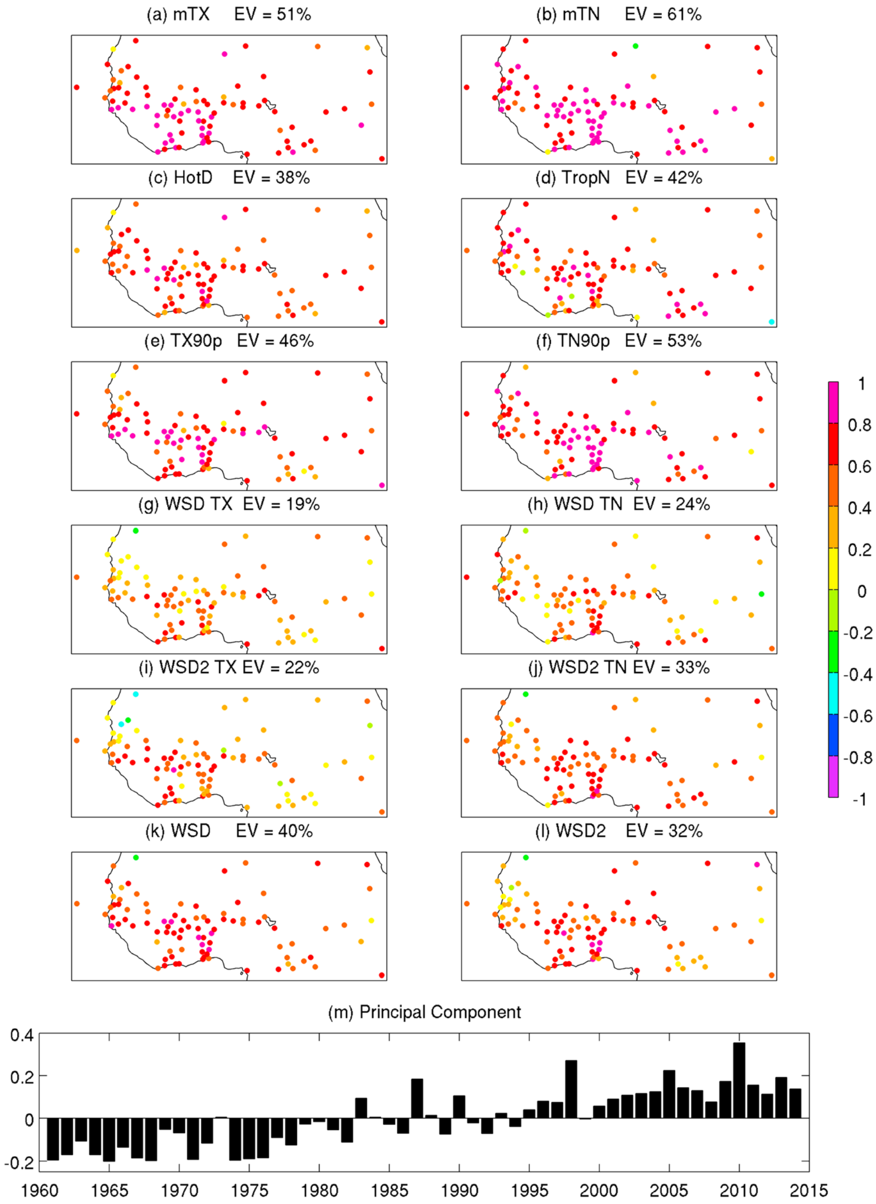

Figure 9. (a–m) Leading EOF mode of standardized anomalies to zero mean and unit variance of annual thermal indices defined in Table 3 combined into a single matrix. The colored dots in Figures 9a–9l are the loadings, represented as the correlations between the leading principal component (Figure 9m) and the indices/stations. The explained variance for each thermal index is labeled in each subtitle and equals the spatial average of squared correlations.

TropN than for annual values (Figure S1). As for annual values, the main changes between the first and last 20-year periods are the significant warming of TX and TN (Figure S2). Even if there is a slight tendency of increased standard deviations, there is not any systematic change in the shape of the PDF as for annual values. In March–June, the trends (Figure S3) are similar to annual values, usually with stronger slopes (especially for WDSs).

4. Modes of Variations and Relationships With Global and Regional Temperatures at Low and High Frequency

4.1. Yearly Values

The preeminence of the long-term trend over interannual variability is clear when all indices are standardized to zero mean and unit variance, then concatenated into a single matrix by columns (with year as observation in rows, and stations and thermal indices as variables in columns), and then subjected to an empirical

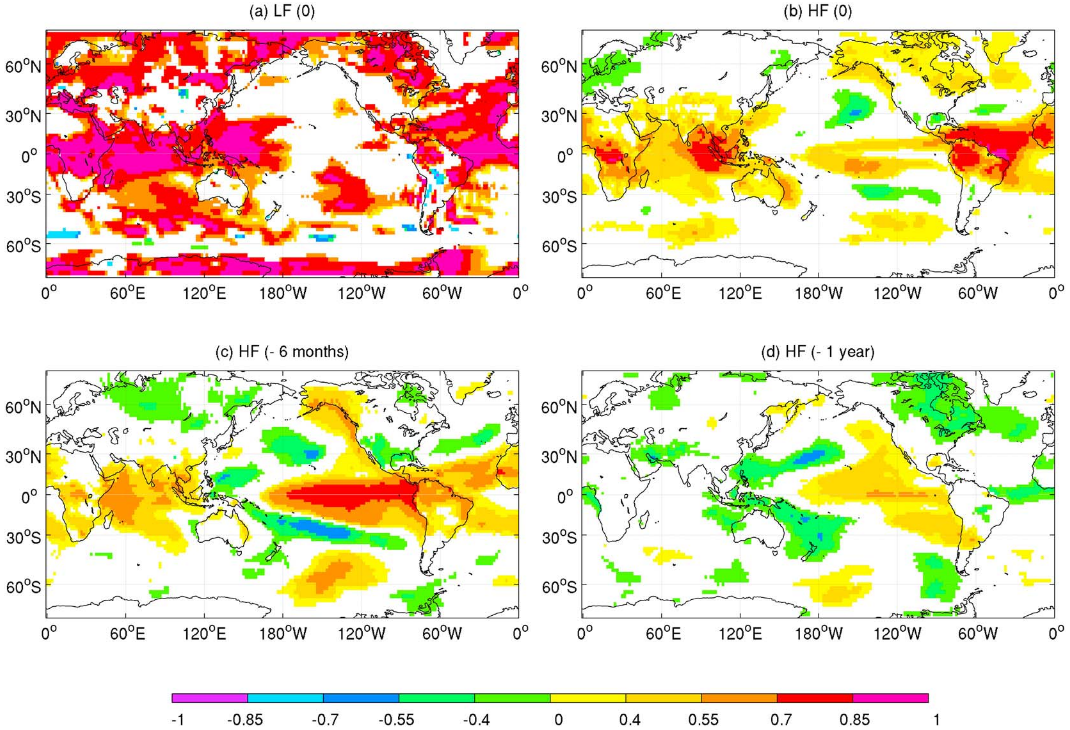

Figure 10. (a) Correlation between the leading EOF mode of low-frequency (>8 years) variations (Figure S4) and the worldwide low-pass (>8 years) annual 2 m temperatures anomalies from NCEP. (b–d) Correlation between the leading EOF mode of high-frequency (<8 years) variations (Figure S5) and the worldwide high-pass (<8 years) annual 2 m temperature anomalies from NCEP : synchronous correlation (Figure 10b); correlations using the July (−1) to June (0) NCEP 2 m temperature anomalies (Figure 10c); correlations using January (−1) to December (−1) NCEP 2 m temperature anomalies (Figure 10d). The white area are not significant at $p = 0.05$ according to a random-phase test [*Janicot et al.*, 1996].

orthogonal function. The first mode explains 36% of the total variance (the second mode, not shown, explains only 6 % of the total variance). The local-scale loadings are almost always positive, indicating a spatially covariant signal (Figure 9). The fraction of explained variance peaks for thermal indices related to TN and usually decreases for WSDs (Figures 9g–9l). As suggested above, considering the consecutive sequences of TN and TX > p90 or P90 increases the signal-to-noise ratio (the leading empirical orthogonal function (EOF) explains therefore more variance in WSD and WSD2 than in WSD TX, WSD TN, and WSD2 TX). The time series (Figure 9m) show negative anomalies until 1982, followed by positive (and increasing) anomalies with clear peaks in 1983, 1987, 1990, 1998, 2005, 2010 (the absolute maximum), and 2013.

We next separate low-frequency variance (LF, slower than 1/8 cycle-per-year) and high-frequency (HF) residuals (i.e., the difference between the total variance and LF) using a recursive Butterworth filter [*Raymond and Garder*, 1991]. The variance conveyed by low frequencies (estimated as the ratio between the LF variance on the sum of LF and HF variances) peaks for mTN (spatial average = 70%) and is usually over 50% except for WSD indices (spatial average between 34% for WSD TX and 47% for WSD2 TN). The first mode of LF variations (Figure S4) is very similar to the first mode shown in Figure 9, except that the fraction of explained variance is logically stronger. The leading mode of HF residuals, shown in Figure S5, shows spatially consistent variations with the same—noisier—variables (mostly WSDs) as previously identified.

Figure 10 shows the correlations between the leading principal component and the LF (Figure S4) and HF (Figure S5) variations of annual 2 m temperature from NCEP/NCAR reanalyses (NCEP hereafter [*Kalnay et al.*, 1996]). The synchronous correlations for LF (Figure 10a) show significant correlations over a large zonal band from the tropical Atlantic to the tropical West Pacific, but also over Antarctica and middle and subpolar latitudes in the Northern Hemisphere. The correlation between the leading LF EOF of thermal indices and the global average of 2 m temperature (red curve in Figure S4) is 0.96. Using regional indices over tropical Atlantic or Indian Ocean leads to slightly weaker correlations (not shown). The long-term variations may be thus viewed as the regional fingerprint of the global warming.

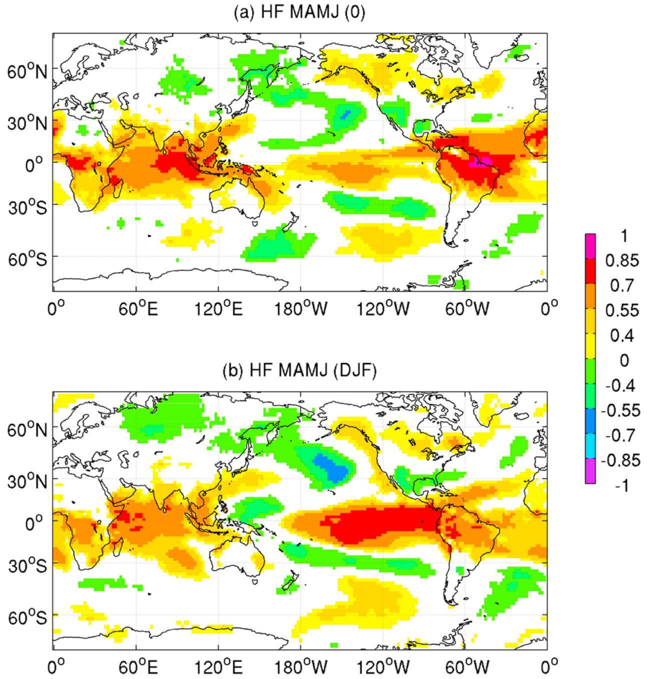

Figure 11. (a) Correlation between the leading high-frequency (<8 years) EOF mode of March–June thermal indices (not shown) and the worldwide high-pass <8 years 2 m temperature anomalies from NCEP in (a) March–June and (b) previous December–February. The white area are not significant at $p = 0.05$ according to a random-phase test [*Janicot et al.*, 1996].

For HF (Figure 10b), a rather zonal symmetric pattern appears with positive correlations over most of tropical zone, peaking from Amazonia to West Africa and the eastern Indian Ocean, while weak negative correlations are found on each side of the positive belt (i.e., in the subtropical latitudes) in both Pacific and Atlantic Oceans. Considering the worldwide thermal anomalies 6 months (i.e., July of year −1 to June of the year 0) (Figure 10c) and 1 year (Figure 10d) before the leading regional HF mode (Figure S5) shows that this variability can be mostly interpreted as the delayed response to large-scale El Niño–Southern Oscillation (ENSO) events. The correlations for a 1-year lag are significant in the tropical Pacific basin, with a classical horseshoe pattern, which suggests that interannual warming (respectively cooling) over tropical Africa tends to follow warm (respectively, cold) ENSO events.

We repeated the analyses for MAMJ warm indices. Even if the loadings change, the leading mode of concatenated unfiltered, LF and HF, standardized anomalies of the 12 indices in MAMJ, is very similar to its annual counterpart (not shown). Figure 11 shows the correlations of the leading HF PC and the MAMJ and December-January-February (DJF) NCEP HF 2 m temperatures. The delayed impact of ENSO events is clear. Note that correlation between the leading HF PC in MAMJ and the HF North Atlantic Oscillation (NAO) index from CPC in MAMJ equals −0.17 (not significant according to a random-phase test), suggesting that NAO does not significantly impact the mean MAMJ thermal conditions. This insignificant correlation contrasts with the significant increase of the daily occurrence of warm days during negative NAO events [*Fontaine et al.*, 2013]. It is possible that seasonal MAMJ mean NAO value does not properly account for daily negative NAO events.

4.2. Retrospective Hindcast of MAMJ Warm Extremes With DJF Sea Surface Temperatures

We use four regional-scale indices that are defined as the spatial average of DJF SST from ERSSTv4 [*Huang et al.*, 2015] over the equatorial Pacific tropical Indian Ocean, tropical North Atlantic, and tropical South Atlantic. Figure 12 shows the correlations between the observed 12 MAMJ indices and the retrospective hindcasts associated with the four regional-scale SST indices. The correlations are based on cross-validated hindcasts from a multilinear regression using DJF SST indices to hindcast the local-scale MAMJ warm indices defined in Table 3. The parameters are trained on the first 53 years and tested on the remaining years. The correlations are especially large over the western Sahel and Guinean Africa (Figure 12) and are close to zero near the central and eastern Sahelian-Sudanian belts for HotD (Figure 12c), while the mean state for these variables is close to constant values (i.e., 122 days) in March–June (not shown). The pattern of correlations for warm spell durations is noisier (Figures 12g–12l), even if correlations are positive for most stations for WSD2 from the interior of Senegal to Chad and more generally over Sudanian and Guinean Africa (Figure 12l).

Tables 4 and 5 show the correlations (for unfiltered and HF variations) for standardized annual anomaly indices (=spatial average of the standardized anomalies, i.e., removing the local mean and dividing by the local standard deviations) over the nine areas defined from Figure 2. The correlations between observations and retrospective predictions are overall significant at $p = 0.05$, especially for Sahelian, Sudanian, and Guinean

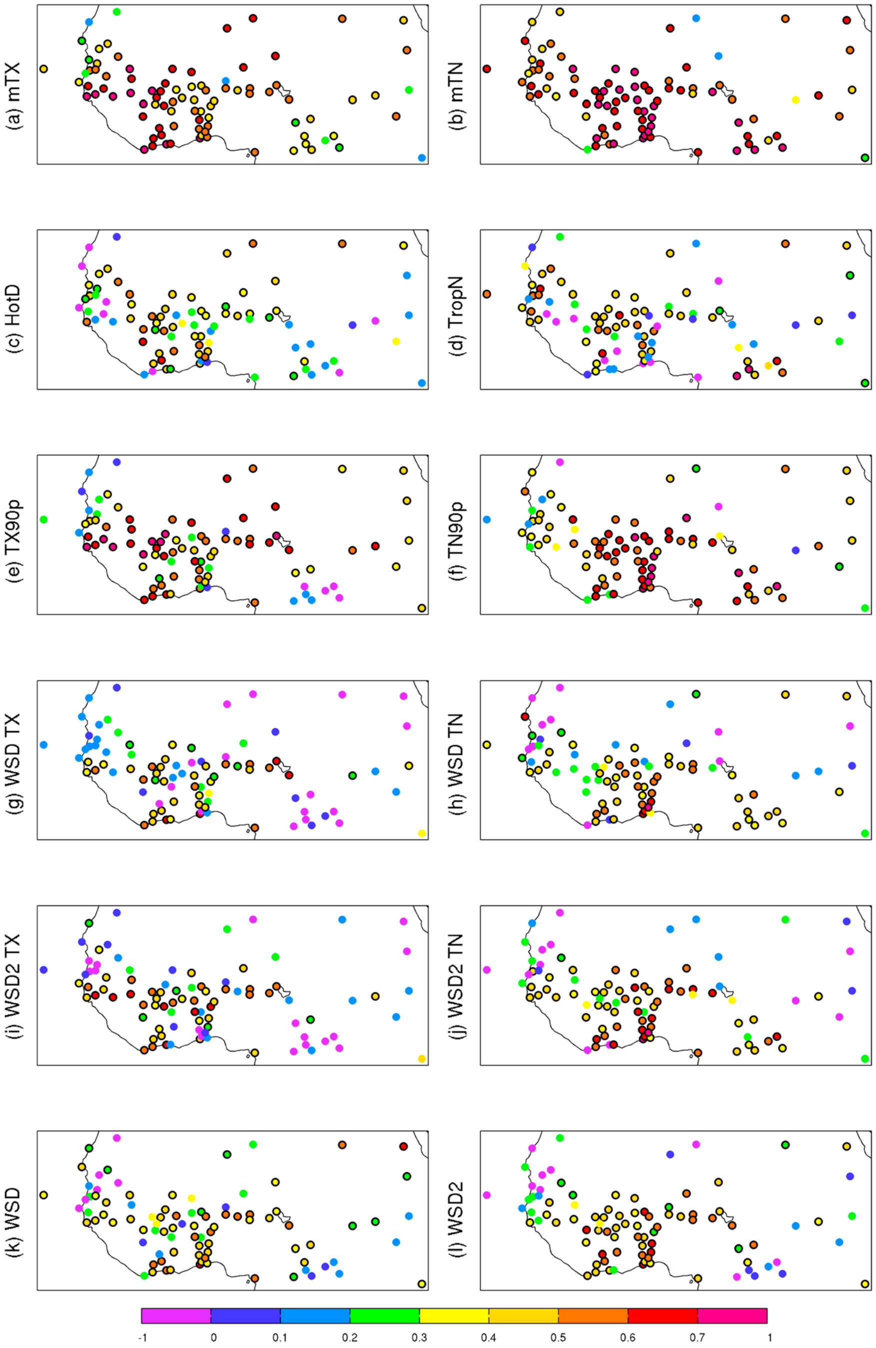

Figure 12. Correlation between the observation and retrospective hindcast of March–June (a) mTX, (b) mTN, (c) HotD, (d) TropN, (e) TX90p, (f) TN90p, (g) WSD TX, (h) WSD TN, (i) WSD2 TX , (j) WSD2 TN, (k) WSD, and (l) WSD2 variations (indices are defined in Table 3). The hindcast are obtained through a cross-validated multilinear regression with the parameter computed on 53 years, while the remaining year is estimated. The predictors are December–February mean sea surface temperatures spatially averaged over four regions (190°E–280°E, 5°S–5°N, equatorial Pacific; 45°E–70°E, 20°S–20°N, tropical Indian Ocean; 70°W–15°W, 0°N–20°N, tropical North Atlantic; and 40°W–10°E, 20°S–0°S, tropical South Atlantic), while the predictands are the local-scale warm indices in March–June. The black circle indicates significant positive correlations at $p = 0.05$ level according to a random-phase test [*Janicot et al.*, 1996].

areas, while it is lower for Atlantic and Coast stations (Tables 4 and 5). Even if the skill originates from the warming trend, which is taken into account here mostly by Indian and tropical Atlantic SST indices, the HF skill (Table 5) remains usually significant at $p = 0.05$, especially for mTN, TX90p, TN90p, and WSDs for Sahelian, Sudanian, and Guinean areas.

Table 4. Correlations Between Observed and Retrospective Hindcasts of Warm Indices (Defined in Table 3) in March–June[a]

	mTX	mTN	HotD	TropN	TX90p	TN90p	WSD TX	WSD TN	WSD2 TX	WSD2 TN	WSD	WSD2
Atlantic	**0.38**	**0.68**		**0.46**		**0.47**	0.22	**0.54**	0.28		**0.37**	
Coast	0.27	**0.45**	**0.34**	0.30	0.30							
Sa-W	**0.59**	**0.70**	**0.49**	**0.66**	**0.52**	**0.58**	**0.36**	**0.39**		**0.47**	**0.50**	
Sa-E	**0.75**	**0.64**	**0.66**	**0.55**	**0.71**	**0.65**	0.38	0.36	0.33	**0.45**	**0.72**	**0.55**
Sh-W	**0.70**	**0.74**	0.44	**0.54**	**0.78**	**0.71**	**0.58**	**0.63**	**0.73**	**0.67**	**0.63**	**0.68**
Sh-E	**0.57**	**0.68**	0.29	**0.43**	**0.73**	**0.72**	**0.68**	**0.49**	**0.61**	**0.62**	**0.72**	**0.65**
Su-W	**0.63**	**0.71**	**0.53**	**0.60**	**0.65**	**0.70**	**0.44**	**0.60**	**0.62**	**0.61**	**0.56**	**0.65**
Su -E	**0.44**	**0.79**	0.26	**0.71**		**0.72**		**0.64**		**0.61**	**0.44**	**0.43**
Guinea	**0.73**	**0.82**	**0.63**	**0.52**	**0.67**	**0.76**	**0.61**	**0.67**	**0.52**	**0.71**	**0.66**	**0.72**

[a] The hindcasts are obtained through a multilinear regression model using four sea surface temperatures indices (190°E–280°E, 5°S–5°N, equatorial Pacific; 45°E–70°E, 20°S–20°N, tropical Indian Ocean; 70°W–15°W, 0°N–0°N, tropical North Atlantic; and 40°W–10°E, 20°S–0°S, tropical South Atlantic) in December–February as predictors of the local-scale warm indices. The multilinear model is cross-validated (the training is made on 53 years, and the hindcast is computed on the remaining year). The correlations are indicated for standardized anomaly indices (=spatial average of standardized anomalies, i.e., removing the local mean and dividing by the local standard deviations, of stations) for the nine regions defined from Figure 2 (Sa-W: Saharan cluster W of 5°E, Sa-E: Saharan cluster E of 5°E, Sh-W: Sahelian cluster W of 5°E, Sh-E: Sahelian cluster E of 5°E, Su-W: Sudanian cluster W of 5°E, Su-E: Sudanian cluster E of 5°E). Values in bold indicate significant positive correlations at $p = 0.01$ according to a random-phase test, while empty cells indicate insignificant correlations at $p = 0.05$.

5. Discussion

We established the climatology and variability of various warm indices (defined in Table 3) for one of the warmest regions on Earth (Figures 2 and 4), where data are either largely absent or too scarce compared to previous gridded analyses based on meteorological stations [*New et al.*, 2006; *Aguilar et al.*, 2009]. The data set of 90 stations (Figure 1) is extracted from two databases, freely available on the web, which were carefully cleaned, cross-checked, and concatenated. A new aspect is the use of PPCA [*Tipping and Bishop*, 1999] to estimate missing entries. PPCA is frequently used to extract eigenvectors from sparse matrix in biology and genetics [*Yu et al.*, 2010; *Nyamundanda et al.*, 2010] but has been rarely used in climate studies. This technique appears to be powerful if the ultimate goal is to reproduce the interannual variability of yearly (or seasonal) warm indices related to the 90th percentile. Dealing with the 90th percentile is less challenging than using for example the yearly (or seasonal) hotter daily TX and TN, which are more sensitive to outliers and sampling uncertainty. The observed data sets include ~25% of missing entries, and ~8.5% of the year-station are fully missing. If we consider the test using 10% of year-station missing as close to the observed case, the mean correlations between observed and reconstructed (including filled daily entries) percentages of TX and TN > P90 and mean length of spells of consecutive TX and TN > P90 are >0.88 (second row of Table 2). Using a percentage of 20% of year-station missing entries leads to correlations >0.78 (third row of Table 3). The reconstruction of warm spell durations is not as accurate as the reconstruction of the percentage of warm days and nights, an expected result since warm spell duration is a rather noisy variable. For instance, the leading eigenvector of the combination of warm indices explains more variance in the percentage of warm days (TX90p) and nights (TN90p) than in warm spell durations (WSDs indices in Table 3). It is also possible that PPCA fails, at least partly, in reproducing the exact chronology of p90/P90 exceedance. The overall quality

Table 5. Same as Table 4 Except for High-Frequency (Faster Than 8 Years) Variations

	mTX	mTN	HotD	TropN	TX90p	TN90p	WSD TX	WSD TN	WSD2 TX	WSD2 TN	WSD	WSD2
Atlantic	**0.35**	**0.48**				**0.33**		**0.38**				
Coast			**0.38**									
Sa-W	0.37	**0.50**		0.32	**0.37**	**0.48**	**0.38**			**0.41**	0.33	
Sa-E	**0.46**	**0.35**	**0.43**	0.30	**0.45**	**0.43**					**0.47**	
Sh-W		**0.58**			**0.49**	**0.53**	**0.43**	**0.51**	**0.49**	**0.60**	0.35	**0.48**
Sh-E	0.34	0.39			**0.57**	**0.50**	**0.50**	0.31	**0.44**	**0.52**	**0.54**	**0.42**
Su-W		**0.60**		0.33	**0.44**	**0.61**	0.33	**0.49**	**0.46**	**0.62**	0.29	**0.52**
Su -E		**0.71**		**0.53**		**0.63**		**0.51**		**0.47**		**0.43**
Guinea	**0.43**	**0.76**	**0.48**		**0.50**	**0.68**	0.28	**0.53**	0.30	**0.62**	**0.42**	**0.57**

of the PPCA reconstruction is indeed related to the concentration of the whole variance in the leading eigen modes. Noisy variations may be impossible to reproduce, at least with this method.

We assume that filling isolated missing entries would not significantly alter the interannual variability of reconstructed annual or seasonal sequences. We may conclude that despite a large amount of missing data, our PPCA reconstruction leads to unobserved but consistent values. Nevertheless, the synthetic time series may fail to reproduce local variations (or real change points), since the PPCA considers only the regional-scale variations explained by the leading eigenvectors. Even if the 30 leading eigenvectors are used here, this potential issue cannot be excluded. Yet we deal here mostly with regional-scale patterns or spatially averaged indices, which are probably less sensitive to this issue. One should be more careful when single daily records are analyzed. In summary, PPCA appears to be a promising tool to fill missing entries and create realistic regional-scale variations of extremes related to 90th percentile, thus allowing a global analysis of upper (or lower) tail of distribution of moderate extremes, including areas with a large percentage of missing entries as here. The quality of the PPCA reconstruction needs to be carefully quantified for stronger extremes than p90/P90, as 95th or 99th (or higher) percentiles or the annual warmest day. But, as suggested above, any value occurring at small scales would be difficult, or even impossible, to accurately reproduce with PPCA. From a climatic perspective, such a local-scale event would have neither a regional nor a global-scale significance.

For most of the region, a clear picture of climate change emerges (Figures 4–6 and 8). The mean annual TX (mTX) and related warm indices (i.e., hot days, warm days with TX $>$ p90, mean warm spell duration, based on TX) show a smooth increase equivalent to ~ +0.021°C/yr in mean for mTX since 1961. The mean annual TN (mTN) and related warm indices show a more step-like variation, with increased rates from 1980 to the mid-1990s, equivalent to a linear increase of ~ +0.028°C/yr in mean since 1961. The warming is overall consistent with a simple shift of the PDF of TX and TN without any clear and systematic changes in its shape (the statistical moments of order $>$1 do not show significant changes between the first and last 20 years, except for a larger standard deviation in 1995–2014 versus 1961–1980 for 30%–40% of the stations; Figure 6). The mean warm spell duration, either estimated from p90 or P90, displays noisier variations than mean TX and TN, hot days, and tropical nights, warm days, and nights. The average warm spell durations are indeed small (usually less than 2–3 days; Figure 3). Exceeding p90 or P90 is thus rarely observed locally on consecutive days, even if some recent years (mostly 1998 and 2010) comprise many days included in heat waves lasting at least six consecutive days (Figure 5), especially during the warmest (boreal spring) season across the Sahelian and Sudanian belts.

The physical causes of warming include the modification of radiative balance, which is dominated by the slow planetary increase of greenhouse gases, but also includes local to regional-scale changes in atmospheric moisture and aerosol's loadings in addition to variations in cloudiness. We have no means to differentiate the urbanization effect related to urban growth in these trends since there are no reliable records of population since the 1960s, except for large cities (as Dakar or Niamey). Gridded global population products (http://sedac.ciesin.columbia.edu/data/collection/gpw-v3) are available from 1990 only. It is clear that large cities quickly developed since the 1960s–1970s and the urbanization effect is most likely equivalent for these cities to the effect observed elsewhere. Another class of physical causes is the change in advection-convection processes. In particular, TX is impacted by the vertical mixing in the boundary layer. The low-frequency variations ($>$8 years) of thermal indices may be largely related to global warming. The strong covariance with Tropical Atlantic and Indian basins (Figure 10a) at these time scales suggests either a regional-scale fingerprint of the global warming or a multidecadal regional-scale signal not necessarily related to the recent and ongoing radiative imbalance. In particular, we cannot exclude that part of the low-frequency variations is not related to (multi)decadal modes of variability in the Atlantic and Indian basins. In other words, through the statistics, we cannot attribute the whole low-frequency variations $>$8 years solely to the global warming.

The high-frequency variations $<$8 years clearly show a delayed (3 to 4 months) regional response to Pacific ENSO events (Figures 10c and 10d and 11). The delayed impact could be associated with myriad processes. First of all, it is well established that during a warm ENSO event, anomalous diabatic heating over central and eastern tropical Pacific associated with anomalous deep convection is spread eastward by equatorial Kelvin waves and westward by Rossby waves in the upper troposphere [*Pahri et al.*, 2016]. The anomalous subsidence tends to warm up the tropical troposphere remotely by a few weeks to a few months after the peak of warm ENSO events [*Klein et al.*, 1999; *Pahri et al.*, 2016]. This large-scale process tends to increase the global mean temperature by few tenths of degrees [*Rahmstorf et al.*, 2012]. In that context, northern tropical Africa could be viewed as an especially strong regional-scale fingerprint of this upper-layer atmospheric bridge. There are also ENSO impacts on the lower troposphere. In the tropical North Atlantic, the trade winds are reduced during boreal spring after a warm ENSO peak, decreasing the latent heat flux and enhancing the net heat flux toward the ocean, and thus warming its mixed-layer [*Klein et al.*, 1999]. This anomalous heat could be advected by the low level winds toward Sahel-Sudan (B.Oueslati et al., Characterisation of heat waves in the Sahel and associated mechanism, submitted to *Journal of Climate*, 2016). Hence, ENSO impacts could be transmitted jointly through the upper and lower tropical troposphere. This teleconnection is especially relevant for boreal spring for two independent reasons: (i) it is the warmest season of the year across the Sahelian and Sudanian belts and (ii) it lags the usual mature phase of ENSO events. Our simple multilinear regression of local-scale thermal indices in MAMJ from DJF antecedent SST in the tropical oceans (Figure 12 and Tables 4 and 5) offers thus promising prevision skill, especially for TN-related indices and usually lower skill along the Tropical North Atlantic.

Model-based projections of future greenhouse gas-induced climate change for this domain suggest that the warming will continue in the forthcoming decades [*Hulme et al.*, 2001]. The annual mean warming in 2080 (relatively to 1961–1990 mean) could be comprised between 1.4°C and 2°C for a low radiative forcing (Representative Concentration Pathway (RCP) 2.6) and 4.9°C to 6.8°C for an high one (RCP 8.5). Regional climate model projections also show that future warming is likely to be particularly strong (up to 3°C per 50 year between 2001 and 2050) in the Sahelian-Sudanian belts [*Paeth et al.*, 2009]. Such an increase could be detrimental for humans and ecosystems due to the already warm mean state. Even if projections of extreme temperatures remain speculative, the spatial ratio between mTX and mTN trends and temperature extremes (Figure 7) allows a simple temporal extrapolation: for example a mean increase of 2°C of mTX could be related to approximately +75 hot days with $TX > 35°C$ per year (giving an average of ~300 days per year for Sahelian stations), +0.3 proportion of warm days, and +1 day of heat spell duration. Such an exercise is less trivial for mTN and related temperature indices, since the relationships between mTN and related warm extremes are less linear (Figure 7). Nevertheless, this seriously raises the issue of the habitability of this region, or, in other words, whether persisting warm temperatures will become intolerable for humans, without an efficient adaptation, especially during the warmest period of the year and synchronous to the ending phases of warm ENSO events. In the future, could the Sahelian and Sudanian belts become regions incompatible, at least temporarily, with permanent human settlements?

6. Concluding Remarks

Mean temperature and warm extreme indices have been analyzed for tropical Africa north of equator and west of 36°E for annual values and specifically for the March-June season, the warmest of the year over most of the area. The statistical analyses are derived from daily maximum (TX) and minimum (TN) temperature based on 90 in situ observational records over the 1961–2014 period, completing global analyses [*Groisman et al.*, 1999; *Frich et al.*, 2002; *Alexander et al.*, 2006; *Christidis et al.*, 2005; *Brown et al.*, 2008; *Donat et al.*, 2013a]. Current trends of mean TX and TN range usually between +2°C and +3°C per century, and this warming should be viewed merely as a shift of the PDF of daily TX and TN without any systematic change of the shape of the PDF except for an increase of the standard deviation in the last 20 years versus the first ones for 30%–40% of stations. The frequencies of hot days ($TX > 35°C$) and tropical nights ($TN > 20°C$), as well as the frequencies of warm days ($TX > p90$) and nights ($TN > p90$), follow roughly the trends of mean TX and TN, even if several stations tend to be already close to absolute maxima (as for hot days in March–June across the Sahel and Sudanian belts or yearly tropical nights over Guinean Africa). The mean duration of warm spells (consecutive TX or TN or both TX and $TN > p90$ or P90) is short, since a lot of warm days or nights are indeed isolated, and its interannual variations are noisier than those of mean TX and TN and related frequencies of hot days and similar metrics. Nevertheless, the mean duration increases clearly with far more heat waves lasting at least six consecutive TX or TN or both TX and $TN > p90$ from 1998 onward. Overall, warming trends are weaker along the North Tropical Atlantic. The low-frequency (>8 years) variations roughly follow the global warming even if multidecadal variations over Atlantic and Indian oceans may play an additional role. High-frequency (<8 years) variations are tightly related to ENSO events, with warm events in the Pacific tending to be followed by warmer temperatures over northern tropical Africa after a few months delay. This relationship is particularly useful for the prediction of boreal spring (March–June) temperature anomalies, since this season combines the warmest annual temperatures across Sahelian and Sudanian belts and lags the usual peak of ENSO events in boreal winter. We can thus anticipate severe warm conditions in MAMJ 2016 related to the warm ENSO event that reached its highest amplitude during the 2015–2016 boreal winter.

Acknowledgments
This study is a part of ANR project ACASIS (2014–2017, grant: ANR-13-SENV-0007). The temperature data sets have been obtained free of charge from http://www7.ncdc.noaa.gov/CDO/cdoselect.cmd?datasetabbv=GSOD&countryabbv=&georegionabbv= (GSOD data set) and from https://www.ncdc.noaa.gov/oa/climate/ghcn-daily/ (GHCN data set). The authors thank three anonymous reviewers and the Associate Editor (C. Zhang) for their constructive comments that helped improve the manuscript. We also thank Teddy Allen (IRI, Columbia University) for his careful proofreading of the revised version of this paper. and Emilie Bernard for preliminary analyses.

References

Aguilar, E., et al. (2009), Changes in temperature and precipitation extremes in western central Africa, Guinea Conakry and Zimbabwe, 1955–2006, *J. Geophys. Res.*, *114*, D02115, doi:10.1029/2008JD011010.

Alexander, L. V., et al. (2006), Global observed changes in daily climate extremes of temperature and precipitation, *J. Geophys. Res.*, *111*, D05109, doi:10.1029/2005JD006290.

Alexandersson, H., and A. Moberg (1997), Homogenization of Swedish temperature data. Part I: Homogeneity test for linear trends, *Int. J. Climatol.*, *17*, 25–34, doi:10.1002/(SICI)1097-0088(199701)17:1<25::AID-JOC103>3.0.CO;2-J.

Braganza, K., D. J. Karoly, and J. M. Arblaster (2004), Diurnal temperature range as an index of global climate change during the twentieth century, *Geophys. Res. Lett.*, *31*, L13217, doi:10.1029/2004GL019998.

Brown, S. J., J. Caesar, and C. A. T. Ferro (2008), Global changes in extreme daily temperature since 1950, *J. Geophys. Res.*, *113*, D05115, doi:10.1029/2006JD008091.

Caesar, J., L. Alexander, and R. Vose (2006), Large-scale changes in observed daily maximum and minimum temperatures: Creation and analysis of a new gridded dataset, *J. Geophys. Res.*, *111*, D05101, doi:10.1029/2005/JD006280.

Christensen, J. H., et al. (2007), Regional climate projections, in *Climate Change, 2007: The Physical Science Basis. Contribution of Working group I to the Fourth Assessment Report of the Intergovernmental Panel on Climate Change*, chap. 11, pp. 847–940, Cambridge, Univ. Press.

Christidis, N., P. A. Stott, S. Brown, G. C. Hegerl, and J. Caesar (2005), Detection of changes in temperature extremes during the second half of the 20th century, *Geophys. Res. Lett.*, *32*, L20716, doi:10.1029/2005GL023885.1.

Collins, J. M. (2011), Temperature variability over Africa, *J. Clim.*, *24*, 3649–3666, doi:10.1175/2011JCLI3753.1.

Cook, K. H., and E. K. Vizy (2015), Detection and analysis of an amplified warming of the Saharan desert, *J. Clim.*, *25*, 6560–6580, doi:10.1175/JCLI-D-14-00230.1.

Coumou, D., and S. Rahmstorf (2012), A decade of weather extremes, *Nat. Clim. Change*, *2*, 491–496, doi:10.1038/nclimate1452.

Cowan, T., A. Purich, S. Perkins, A. Pezza, G. Boschat, and K. Sadler (2014), More frequent, longer, and hotter heat waves for Australia in the twenty-first century, *J. Clim.*, *27*, 5851–5871, doi:10.1175/JCLI-D-14-00092.1.

Donat, M. G., and L. V. Alexander (2012), The shifting probability distribution of global daytime and night-time temperatures, *Geophys. Res. Lett.*, *39*, L14707, doi:10.1029/2012GL052459.

Donat, M. G., et al. (2013a), Updated analyses of temperature and precipitation extreme indices since the beginning of the twentieth century: The HadEX2 dataset, *J. Geophys. Res. Atmos.*, *118*, 2098–2118, doi:10.1002/jgrd.50150.

Donat, M. G., L. V. Alexander, H. Yang, I. Durre, R. Vose, and J. Caesar (2013b), Global land-based datasets for monitoring climatic extremes, *Bull. Am. Meteorol. Soc.*, *94*, 997–1006.

Donat, M. G., et al. (2014), Changes in extreme temperature and precipitation in the Arab region: Long-term trends and variability related to ENSO and NAO, *Int. J. Climatol.*, *34*, 581–592, doi:10.1002/joc.3707.

Easterling, D. R., J. J. Evans, P. Y. Groisman, T. R. Karl, K. E. Kunkel, and P. Ambenje (2000a), Observed variability and trends in extreme climate events: A brief review, *Bull. Am. Meteorol. Soc.*, *81*, 417–425, doi:10.1175/1520-0477(2000)081%3C0417:OVATIE%3E2.3.CO;2.

Easterling, D. R., G. A. Meehl, C. Parmesan, S. A. Changnon, T. R. Karl, and L. O. Mearns (2000b), Climate extremes: Observations, modeling, and impact, *Science*, *289*, 2068–2074, doi:10.1126/science.289.5487.2068.

Fontaine, B., S. Janicot, and P.-A. Monerie (2013), Recent changes in air temperature, heat waves occurrences and atmospheric circulation in Northern Africa, *J. Geophys. Res. Atmos.*, *118*, 8536–8552, doi:10.1002/jgrd.50667.

Fraedrich, K., C. Ziehmann, and F. Sielmann (1995), Estimates of spatial degrees of freedom, *J. Clim.*, *8*, 361–369, doi:10.1175/1520-0442(1995)008<0361:EOSDOF>2.0.CO;2.

Frich, P., L. V. Alexander, P. Della-Martin, B. Gleason, M. Haylock, A. M. G. Klein Tank, and T. C. Peterson (2002), Observed coherent changes in climatic extremes during the second half of the twentieth century, *Clim. Res.*, *19*, 193–212, doi:10.3354/cr019193.

Groisman, P. Y., et al. (1999), Changes in the probability of heavy precipitation: Important indicators of climate change, *Clim. Change*, *42*, 243–283.

Hartmann, D. L., et al. (2013), Observations: Atmosphere and surface, in *The Physical Science Basis. Contribution of Working Group I to the Fifth Assessment Report of the Intergovernmental Panel on Climate Change*, edited by T. F. Stocker et al., pp. 159–254, Cambridge Univ. Press, Cambridge, U. K.

Huang, B., V. F. Banzon, E. Freeman, J. Lawrimore, W. Liu, T. C. Peterson, T. M. Smith, P. W. Thorne, S. D. Woodruff, and H. M. Zhang (2015), Extended reconstructed sea surface temperature version 4 (ERSST.v4). Part I: Upgrades and intercomparisons, *J. Clim.*, *28*, 911–930.

Hulme, M., R. Doherty, T. Ngara, M. New, and D. Lister (2001), African climate change: 1900–2100, *Clim. Res.*, *17*, 145–168, doi:10.3354/cr017145.

Intergovernmental Panel on Climate Change (2013), *The Physical Science Basis. Contribution of Working Group I to the Fifth Assessment Report of the Intergovernmental Panel on Climate Change*, edited by T. F. Stocker et al., 1535 pp., Cambridge Univ. Press, Cambridge, U. K., and New York.

Janicot, S., V. Moron, and B. Fontaine (1996), Sahel droughts and ENSO dynamics, *Geophys. Res. Lett.*, *23*, 515–518, doi:10.1029/96GL00246.

Kalnay, E., et al. (1996), The NCEP/NCAR 40-year reanalysis project, *Bull. Am. Meteorol. Soc.*, *77*, 437–471, doi:10.1175/1520-0477(1996)077<0437:TNYRP>2.0.CO;2.

King'uyu, S. M., L. A. Ogallo, and E. K. Anyamba (2000), Recent trends of minimum and maximum surface temperatures over Eastern Africa, *J. Clim.*, *13*, 2876–2886, doi:10.1175/1520-0442(2000)013<2876:RTOMAM>2.0.CO;2.

Kjellstrom, T. (2009), Climate change, direct heat exposure, health and well-being in low and middle-income countries, *Global Health Action*, *2*, doi:10.3402/gha.v2i0.1958.

Klein, S. A., B. J. Soden, and N. C. Lau (1999), Remote sea surface temperature variations during ENSO: Evidence for a tropical atmospheric bridge, *J. Clim.*, *12*, 917–932, doi:10.1175/1520-0442(1999)012<0917:RSSTVD>2.0.CO;2.

Klein Tank, A. M. G., and G. P. Können (2003), Trends of indices of daily temperature and precipitation extremes in Europe, 1946–1999, *J. Clim.*, *16*, 3665–3680, doi:10.1175/1520-0442(2003)016<3665:TIODT>2.0.CO;2.

Lott, N., R. Vose, S. A. Del Greco, T. Ross, S. Worley, and J. Comeaux (2008), The integrated surface database: Partnerships and progress, in *Proceedings of 88th AMS Annual Meeting, New Orleans, LA, 20–24 January 2008*, pp. 1–3, Am. Meteorol. Soc, New Orleans.

Menne, M. J., I. Durre, R. S. Vose, B. E. Gleason, and T. G. Houston (2012), An overview of the global historical climatology network daily database, *J. Atmos. Oceanic Technol.*, *29*, 897–910.

Moron, V., A. W. Robertson, M. N. Ward, and P. Camberlin (2007), Spatial coherence of tropical rainfall at regional scale, *J. Clim.*, *20*, 5244–5263, doi:10.1175/2007JCLI1623.1.

New, M., et al. (2006), Evidence of trends in daily climate extremes over southern and west Africa, *J. Geophys. Res.*, *111*, D14102, doi:10.1029/2005JD006289.

Nyamundanda, G., L. Brennan, and I. C. Gormley (2010), Probabilistic principal component analysis for metabolomic data, *BMC Bioinf.*, *11*, 571, doi:10.1186/1471-2105-11-571.

Pachauri, R. K., and A. Reisinger (Eds.) (2008), *Bilan 2007 des Changements Climatiques: Rapport de Synthèse*, 103 pp., GIEC, Geneva, Switzerland.

Paeth, H., K. Born, R. Girmes, R. Podzun, and D. Jacob (2009), Regional climate change in tropical and northern Africa due to greenhouse forcing and land use changes, *J. Clim.*, *22*, 114–132, doi:10.1175/2008JCLI2390.1.

Pahri, P., A. Giannini, P. Gentine, and U. Lall (2016), Resolving contrasting regional rainfall responses to El Nino over Tropical Africa, *J. Clim.*, *29*, 1461–1476, doi:10.1175/JCLI-D-15-0071.1.

Peterson, T. C., C. Folland, G. Gruza, W. Hogg, A. Mokssit, and N. Plummer (2001), Report on the activities of the workin group on climate change detection and related rapporteurs, WMO, Rep. WCDMP-47, WMO-TD 1071, Geneva, Switzerland, 143 pp.

Rahmstorf, S., G. Foster, and A. Cazenave (2012), Comparing climate projections to observations up to 2011, *Environ. Res. Lett.*, *7*, 011006, doi:10.1088/1748-9326/7/4/044035.

Raymond, W. H., and A. Garder (1991), A review of recursive and implicit filters, *Mon. Weather Rev.*, *119*, 477–495.

Ringard, J., et al. (2016), The intensification of thermal extremes in West Africa, *Global Planet. Change*, doi:10.1016/j.gloplacha.2015.12.009, in press.

Rome, S., G. Caniaux, J. Ringard, B. Dieppois, and A. Diedhiou (2015), Identification de tendances récentes et ruptures d'homogénéité des températures: Exemple en Afrique de l'Ouest et sur le Golfe de Guinée, *Publ. AIC*, *28*, 591–596.

Ruggieri, E. (2012), A Bayesian approach to detecting change points in climatic records, *Int. J. Climatol.*, doi:10.1002/joc.3447.

Schär, C., and G. Jendritzky (2004), The European heatwave of 2003: Was it merely a rare meteorological event or a first glimpse of climate change to come?, *Nature*, *432*, 559–560, doi:10.1038/432559a.

Sherwood, S. C., and M. Huber (2010), An adaptability limit to climate change due to heat stress, *Proc. Natl. Acad. Sci. U.S.A.*, *107*, 9552–9555, doi:10.1073/pnas.0913352107.

Stocker, T. F., et al. (2013), *Climate Change 2013.The Physical Science Basis. Working Group I Contribution to the Fifth Assessment Report of the Intergovernmental Panel on Climate Change-Abstract for Decision-makers*, 1552 pp., WMO, Geneva, Switzerland.

Tipping, M. E., and C. M. Bishop (1999), Probabilistic principal component analysis, *J. R. Stat. Soc., Ser. B*, *61*, 611–622.

Trigo, R. M., R. García-Herrera, J. Díaz, I. F. Trigo, and M. A. Valente (2005), How exceptional was the early August 2003 heatwave in France? *Geophys. Res. Lett.*, *32*, L10701, doi:10.1029/2005GL022410.

Wang, X. L. (2008), Accounting for autocorrelation in detecting mean- shifts in climate data series using the penalized maximal t or F test, *J. Appl. Meteorol. Climatol.*, *47*, 2423–2444.

Wingaard, J. B., A. M. G. Klein Tank, and G. P. Können (2003), Homogeneity of 20th century European daily temperature and precipitation series, *Int. J. Climatol.*, *23*, 679–692, doi:10.1002/joc.906.

Yu, M., R. R. Snapp, T. Ruiz, and M. Rademacher (2010), Probabilistic principal component analysis with expectation maximization (PPCA-EM) facilitates volume classification and estimates the missing data, *J. Struct. Biol.*, *171*, 18–30, doi:10.1016/j.jsb.2010.04.002.

Zhang, X., L. Alexander, G. C. Hegerl, P. Jones, A. M. G. Klein Tank, T. C. Peterson, B. Trewin, and F. W. Zwiers (2011), Indices for monitoring changes in extremes based on daily temperature and precipitation data, *Wiley Interdiscip. Rev. Clim. Change*, *2*, 851–870, doi:10.1002/wcc.147.